SCIENCE CHINA
Information Sciences

• RESEARCH PAPER •

November 2026, Vol. 69, Iss. 11, 210304:1–210304:21
https://doi.org/10.1007/s11432-026-5187-8

Special Topic: Communication, Sensing, and Target Recognition for Low-Altitude Economy

# Optimal sparse conformal array design for dual-polarized weather radar with integrated communications in low-altitude airspace

Weitong ZHAI[1,2], Xiangrong WANG[1*], Jun ZHANG[3], Jindong XIE[1], Kaiquan CAI[1] & Xianbin CAO[1]

[1]*School of Electronic and Information Engineering, State Key Laboratory of CNS/ATM, Beihang University, Beijing 100191, China*
[2]*Department of Electrical and Computer Engineering, National University of Singapore, Singapore 117583, Singapore*
[3]*Advanced Research Institute of Multidisciplinary Science, Beijing Institute of Technology, Beijing 100081, China*

Received 14 March 2026/Revised 25 August 2026/Accepted 21 September 2026/Published online 26 October 2026

**Abstract** The safety and efficiency of the low-altitude economy (LAE) are highly dependent on high-fidelity, real-time awareness of micro-scale meteorological conditions. Hazardous low-altitude weather phenomena, such as localized wind shear and intense precipitation, pose significant risks to unmanned aerial vehicle (UAV) operations. This paper investigates an airship-borne dual-polarized weather radar system with integrated sensing and communication (ISAC) capabilities, designed to provide persistent, high-resolution monitoring of the low-altitude atmospheric environment. To reconcile the requirements for large-aperture sensing with the aerodynamic and payload constraints of low-altitude platforms, we propose a joint design of a sparse conformal array and beamforming. A dual-polarized conformal detection model is established to extract high-resolution polarimetric signatures, which are essential for detecting hazardous weather in complex low-altitude terrains. Leveraging this model, a polarized transmit beampattern modulation scheme is developed to embed critical flight-safety data into polarization components, enabling a threefold increase in data rate for air-to-ground and air-to-air coordination. The joint optimization of the sparse array configuration and beamformer is formulated as a multivariate combinatorial problem and solved using the alternating direction method of multipliers (ADMM). This ensures robust performance across diverse scanning angles required for wide-area low-altitude surveillance. Simulation results, including multi-channel meteorological echoes based on WSR-88D data, demonstrate that the proposed system achieves superior performance in both sensing accuracy and communication throughput, offering a viable solution for the integrated sensing and communication infrastructure essential to the low-altitude economy.

**Keywords** dual-polarized weather radar, low-altitude airspace, integrated sensing and communications, sparse conformal array design

**Citation** Zhai W T, Wang X R, Zhang J, et al. Optimal sparse conformal array design for dual-polarized weather radar with integrated communications in low-altitude airspace. Sci China Inf Sci, 2026, 69(11): 210304, https://doi.org/10.1007/s11432-026-5187-8

## 1 Introduction

Ensuring the safety and efficiency of the low-altitude economy (LAE) demands real-time, high-precision monitoring of micro-scale meteorological conditions, placing unprecedented requirements on weather radar systems [1–3]. For applications such as urban air mobility and drone logistics, operational safety hinges on the accurate detection of abrupt, highly localized weather hazards within the lower atmospheric boundary layer, including wind shear and microbursts. While legacy radars like the WSR-88D established foundational capabilities [4, 5], their mechanical scanning mechanisms lack the agility for the fine-grained, minute-to-second update rates now required. To overcome the limitations of mechanical inertia, phased array radars offer a robust solution through agile electronic beam steering [6, 7]. Building upon this paradigm, conformal array radars further advance detection capabilities [8–10]. By integrating antennas onto the curved surfaces of aerial platforms like tethered balloons and airships, these systems enable large-aperture detection and prolonged station-keeping without compromising aerodynamic performance.

In terms of meteorological detection systems, dual-polarized technology has become a core component of modern weather radars [11, 12]. By transmitting and receiving orthogonal horizontal ($H$) and vertical ($V$) signals, dual-polarized systems derive key variables—including differential reflectivity ($Z_{DR}$), differential phase ($\phi_{DP}$), and copolar correlation coefficient ($\rho_{HV}$)—that substantially improve microphysical characterization [13], precipitation

* Corresponding author (email: xrwang@buaa.edu.cn)

© Science China Press 2026 

estimation [14], and clutter discrimination [15]. Among the two primary operational modes, alternating transmission of horizontal and vertical polarization (AHV) and simultaneous transmission and reception of both polarizations (SHV) [16–18], the latter offers distinct advantages. By transmitting dual-polarized signals simultaneously, SHV eliminates temporal decorrelation inherent in polarization switching, ensures self-consistency of polarimetric variables during rapidly evolving precipitation, simplifies transceiver design by removing the need for high-speed polarization switches, and supports higher pulse repetition frequencies for faster data updates, thereby meeting the stringent temporal resolution requirements for severe weather monitoring [18–20].

Accordingly, this paper investigates an airship-borne conformal dual-polarized radar serving the LAE, operating in SHV mode with each element integrating horizontal/vertical dual-polarized feeds. This configuration harnesses both the aerodynamic benefits of conformal integration and the sensing advantages of polarization diversity for high-resolution meteorological detection. However, unlike conventional planar arrays, the conformal curvature introduces distinct electromagnetic challenges. The varying signal incidence angles across elements, combined with the inherent directivity and angle-dependent responses of individual radiators, lead to pronounced element-dependent radiation characteristics. Moreover, variations in the local reference plane across the array induce substantially different polarization responses, amplifying cross-polarization components and introducing non-negligible interference [21–23]. To address these issues, this paper proposes a dual-channel joint transmit-receive beamforming scheme that collaboratively optimizes the excitation weights for both $V$- and $H$-polarization channels. This approach effectively mitigates the challenges posed by element-dependent pattern characteristics and polarization response disparities, providing a viable solution for directional meteorological detection within a conformal dual-polarized architecture.

For airborne platforms, payload capacity imposes a critical design constraint, limiting the number of antenna elements that can be deployed. However, the high angular resolution required for meteorological detection typically necessitates a large array aperture. For uniformly spaced full arrays, this directly translates to a significant increase in element count. Sparse array design offers an effective means to reconcile this trade-off [24–26]. By optimizing spatial element distribution while preserving a large aperture, sparse arrays overcome the limitations of conventional uniform spacing, achieving comparable spatial resolution with substantially fewer elements. Sparse array techniques have garnered considerable attention in meteorological radar applications. Ref. [27] demonstrated that compressive sensing, particularly basis pursuit denoising, enables a 25% reduction in antenna elements for phased array weather radar while maintaining high observation accuracy. Ref. [28] evaluated sparse array radar performance under heavy rain through controlled chamber experiments. Ref. [29] presented a joint design of sparse array configuration and beamforming weights with constant modulus constraints for an airborne phased array weather radar, enabling high-resolution typhoon observation and integrated communications. Despite these advances, sparse optimization has yet to be extended to the more practical scenario of dual-polarized conformal arrays for meteorological detection. This paper addresses this gap by incorporating sparse optimization into dual-polarized conformal array design, aiming to balance detection performance and system cost under the payload constraints of airborne platforms.

In addition to high-precision detection performance, the reliable transmission of collected information to ground control stations or user ends constitutes another critical requirement in system design. A standalone communication device would not only compete for limited spectral resources allocated to weather radar but also introduce electromagnetic compatibility issues due to co-site deployment, while further increasing platform payload and system costs. Integrated sensing and communications (ISAC) offers a viable solution [30–32]. In ISAC systems, beamforming has become a key technique for coordinating sensing and communication performance. Recent studies have investigated ISAC beamforming for diverse application scenarios and design requirements, including multi-user transmit beamforming [33], robust beamforming under channel uncertainty and clutter interference [34], and cooperative multi-BS beamforming jointly optimized with receive filtering and trajectory design [35]. Multi-static cell-free ISAC has also been studied through access-point duplex-mode optimization to balance communication and sensing performance [36]. More recently, ISAC research has moved beyond fixed configurations and passive adaptation toward proactively reshaping the wireless propagation environment and dynamically reconfiguring transceiver hardware. IRS-enabled ISAC realizes propagation-environment shaping through joint transmit and reflective beamforming [37]. At the transceiver, sparse array-assisted ISAC exploits antenna selection and dynamic sparse array reconfiguration to reshape the effective aperture and enlarge the available spatial design space [38]. Emerging reconfigurable antenna architectures, such as movable antennas [39], further extend this design flexibility by enabling adaptive adjustment of antenna positions.

Depending on design priorities, ISAC architectures can be categorized into radar-centric, communication-centric, and joint optimization. Among these architectures, this paper adopts a radar-centric ISAC framework tailored for weather radar applications, wherein radar signals serve as information carriers and communication data is embedded into the shared transmit waveform, enabling data downlink without compromising core sensing functions. Current research on radar-centric ISAC primarily falls into two categories: spatial index modulation and

beampattern modulation. The former maps communication information onto combinations of radar transmission parameters, exemplified by frequency-hopping designs based on carrier agility, or through antenna indexing and antenna-waveform pairing [40–42]. The latter embeds communication information into the radar transmit beampattern via amplitude or phase modulation, supporting signaling schemes such as PSK, ASK, and QAM [43–45]. This paper extends the beampattern modulation paradigm to the polarization domain, proposing a polarization beampattern modulation-based ISAC scheme. By embedding communication information into the beampatterns of different transmit polarization channels, the proposed approach achieves significantly enhanced communication rates while preserving meteorological detection performance, thereby enabling efficient and reliable data downlink.

To the best of our knowledge, this work presents the first optimal dual-polarized sparse conformal array design for weather radar with integrated communications. The main contributions are summarized as follows.

- Propose an airship-borne dual-polarized conformal array-based ISAC system for the LAE, combining sparse array optimization with joint transmit-receive beamforming to simultaneously enable reliable communications and wide-range, narrow-beam scanning for meteorological detection.
- Establish the dual-polarized conformal meteorological detection model, wherein each antenna features a directive beampattern, and propose the polarization-domain transmit beampattern modulation scheme.
- Formulate the joint design of sparse conformal array and beamforming as a multivariate and binary optimization problem, and solve it via the alternating direction method of multipliers (ADMM), yielding a common sparse array layout shared across all scanning angles and the entire communication symbol constellation.
- Simulate multi-channel meteorological echoes and evaluate the proposed sparse dual-polarized conformal array, demonstrating superior detection and communication performance.

The rest of this paper is organized as follows. Section 2 presents the transmit modeling for weather sensing. Section 3 describes the proposed integrated communication and decoding scheme in the polarization domain. Section 4 details the radar receive beamforming design. Section 5 introduces the joint sparse array and beamforming optimization framework. Section 6 provides simulation results, followed by concluding remarks in Section 7.

Notations. In this paper, $(\cdot)^*$, $(\cdot)^{\mathrm{T}}$, $(\cdot)^{\mathrm{H}}$ denote complex conjugation, transpose, and Hermitian transpose, respectively. Bold lowercase letters represent vectors, bold uppercase letters represent matrices, and $[\mathbf{a}]_i$ and $\mathbf{a}[i]$ denote the $i$-th element of $\mathbf{a}$. For vector coordinates, superscript "˜" indicates representation in the local coordinate system, while its absence indicates the global system; subscripts "$_{\mathrm{c}}$" and "$_{\mathrm{s}}$" denote Cartesian and spherical coordinate representations, respectively. Unless otherwise stated, vectors are assumed to be represented in the global Cartesian coordinate system, and the bold letter "$\mathbf{e}$" is specifically used to denote the coordinates of the electric field in different reference coordinate systems.

## 2 Transmit modeling for weather sensing

As illustrated in Figure 1(a), this paper considers an airship-borne dual-function polarized conformal weather radar system with integrated communications. A conformal two-dimensional sparse antenna array is mounted on one side of the airship. The detection region is divided into $P_1$ azimuth bins and $P_2$ elevation bins, yielding a total of $P = P_1 \times P_2$ angular bins. The weather radar embeds communication information while sequentially scanning each bin. With $K$ users and a communication dictionary of length $Q$, the transmitter needs distinct beamforming weights for each angular bin and each dictionary symbol. For simplicity in modeling, this section and Section 3 present the general transmit formulation using the $p$-th angle bin and $q$-th symbol in the dictionary as an illustrative example. **Note that in the expressions for beampatterns and transmit weight vectors, the subscripts denoting angle bin index "$p$" and symbol index "$q$" are omitted for brevity.**

It is worth noting that atmospheric turbulence and wind gusts may induce airship attitude variations and beam pointing deviations. In practical operation, the airship is equipped with attitude control and stabilization systems to mitigate platform variations, while real time attitude and navigation information can be used for beam pointing compensation [46–49]. Accordingly, this work focuses on sparse array configuration and beamforming design under stabilized operating conditions, without explicitly modeling time-varying platform attitude.

Without loss of generality, the signal is assumed to be a transverse electromagnetic (TEM) wave, with the electric field perpendicular to the propagation direction. Sections 2–4 establish the signal models for the full array, while Section 5 addresses the sparse array design. Consider a dual-polarized conformal full array comprising $N = N_1 \times N_2$ antennas (with $N_1$ and $N_2$ being the number of rows and columns), each of which is equipped with two feed channels for transmitting vertical and horizontal polarization waves, referred to as the $V$-port and $H$-port, respectively. The weather radar operates in SHV mode, transmitting and receiving both polarizations simultaneously. All $H$-ports share an identical radiation pattern, with $\theta$- and $\phi$-direction components in the local spherical coordinate system

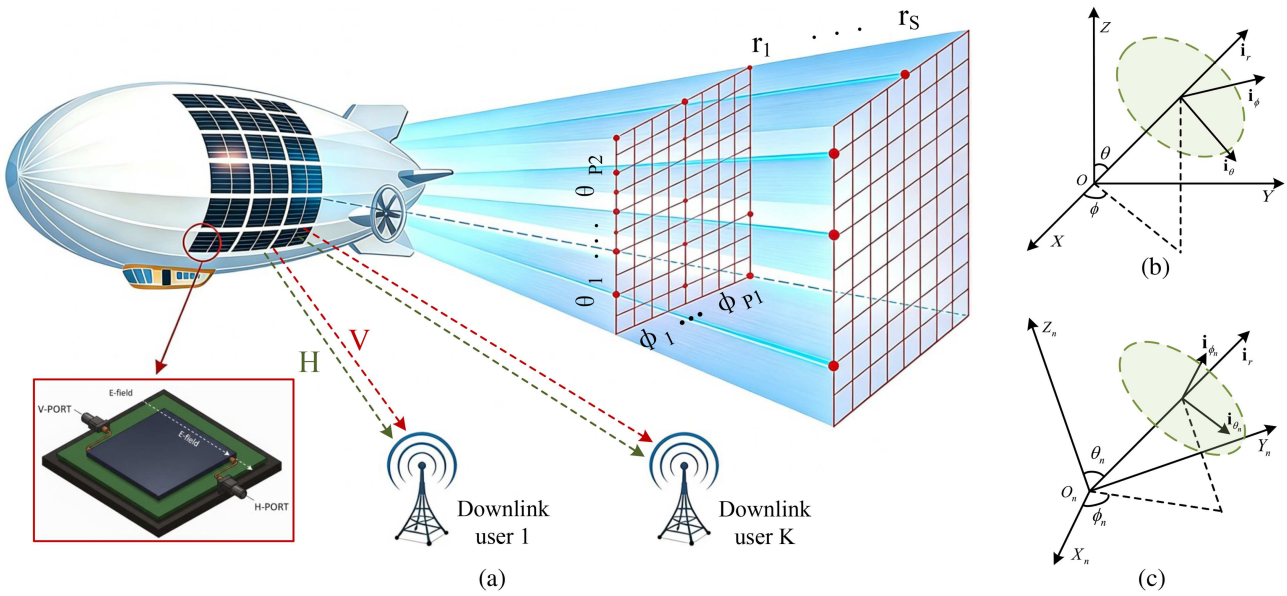


**Figure 1** (Color online) (a) Schematic diagram of the sparse conformal array system for dual-polarized weather radar with integrated communications. Schematic of Cartesian/spherical coordinate systems: (b) global; (c) local (for the $n$-th antenna).

denoted as $G_{H_\theta}(\theta,\phi)$ and $G_{H_\phi}(\theta,\phi)$, where $\theta$ and $\phi$ represent elevation and azimuth angles. Likewise, all $V$-ports share an identical pattern with corresponding components $G_{V_\theta}(\theta,\phi)$ and $G_{V_\phi}(\theta,\phi)$.

### 2.1 Definition of reference coordinate systems

For a conformal array, each antenna element has its own local coordinate system. In this subsection, we first define the global and local Cartesian and spherical coordinate systems as reference frames.

Figure 1(b) illustrates the global Cartesian and spherical systems. In the Cartesian system, the $XOY$-plane is parallel to the ground, with the $z$-axis perpendicular; horizontal and vertical polarizations align with the positive $X$- and $Z$-axes, respectively. In the spherical system, the orthogonal basis consists of propagation direction $\mathbf{i}_r$, elevation direction $\mathbf{i}_\theta$, and azimuth direction $\mathbf{i}_\phi$. For TEM waves, the electric field vector is confined to the plane spanned by $\mathbf{i}_\theta$ and $\mathbf{i}_\phi$, where $\mathbf{i}_\theta$ represents the vertical polarization direction and $\mathbf{i}_\phi$ the horizontal polarization direction. Geometrically, $\mathbf{i}_r$, $\mathbf{i}_\theta$, and $\mathbf{i}_\phi$ can be expressed in terms of

$$\mathbf{i}_r = [\sin\theta\cos\phi, \sin\theta\sin\phi, \cos\theta]^{\mathrm{T}},\ \mathbf{i}_\theta = [\cos\theta\cos\phi, \cos\theta\sin\phi, -\sin\theta]^{\mathrm{T}},\ \mathbf{i}_\phi = [-\sin\phi, \cos\phi, 0]^{\mathrm{T}}. \tag{1}$$

Figure 1(c) defines the local Cartesian and spherical coordinate systems for the $n$-th antenna element. This local Cartesian system is obtained by rotating the global coordinate system counterclockwise through angles $D_n$, $E_n$, and $F_n$ about the $X$-, $Y$-, and $Z$-axes, respectively, with the corresponding rotation matrices denoted as

$$\mathbf{T}_X(D_n) = \begin{bmatrix} 1 & 0 & 0 \\ 0 & \cos D_n & \sin D_n \\ 0 & -\sin D_n & \cos D_n \end{bmatrix},\ \mathbf{T}_Y(E_n) = \begin{bmatrix} \cos E_n & 0 & -\sin E_n \\ 0 & 1 & 0 \\ \sin E_n & 0 & \cos E_n \end{bmatrix},\ \mathbf{T}_Z(F_n) = \begin{bmatrix} \cos F_n & \sin F_n & 0 \\ -\sin F_n & \cos F_n & 0 \\ 0 & 0 & 1 \end{bmatrix}. \tag{2}$$

Within this local Cartesian frame, the horizontal and vertical polarization directions are separately aligned with the positive $X$- and $Z$-axes. The local spherical coordinate system for this element is formed by an orthogonal basis consisting of $\mathbf{i}_r$, the local elevation direction ($\mathbf{i}_{\theta_n}$), and the local azimuth direction ($\mathbf{i}_{\phi_n}$). In this local spherical frame, $\mathbf{i}_{\theta_n}$ is defined as the vertical polarization direction, while $\mathbf{i}_{\phi_n}$ is defined as the horizontal polarization direction. $\mathbf{i}_{\theta_n}$ and $\mathbf{i}_{\phi_n}$ are defined in the same way as (1).

Based on (2), the signal propagation direction $\mathbf{i}_r$ under the $n$-th antenna's local Cartesian coordinate system can be expressed by

$$\tilde{\mathbf{i}}_{r_n,\mathrm{c}} = \mathbf{T}_Z(F_n)\mathbf{T}_Y(E_n)\mathbf{T}_X(D_n)\mathbf{i}_r. \tag{3}$$

Accordingly, the elevation and azimuth angles of $\mathbf{i}_{r_n}$ in the $n$-th local coordinate system can be calculated as

$$\theta_n = \cos^{-1}([\tilde{\mathbf{i}}_{r_n,\mathrm{c}}]_3),\ \ \phi_n = \mathrm{atan2}([\tilde{\mathbf{i}}_{r_n,\mathrm{c}}]_2, [\tilde{\mathbf{i}}_{r_n,\mathrm{c}}]_1), \tag{4}$$

where $\mathrm{atan2}(y, x)$ denotes the four-quadrant inverse tangent for unambiguous azimuth determination.

To enable unified analysis and processing of signals in a conformal array, it is necessary to transform the signals from the local coordinate systems of each element to the global coordinate system. Suppose the transmit power of each port, whether horizontally or vertically polarized, on every antenna is $P_T$. In the following, we describe how to convert local signals to global signals and perform transmit beamforming.

### 2.2 Transmit beamforming for weather sensing

For the $n$-th antenna, the complex electric field vector of the TEM wave at time $t$, which is perpendicular to the propagation direction $\mathbf{i}_r$, can be expressed as

$$\mathbf{s}_{V_n}(t) = \sqrt{P_T} u_V(t) \mathrm{e}^{\mathrm{j}2\pi f_0 t} [G_{V_\theta}(\theta_n, \phi_n)\mathbf{i}_{\theta_n} + G_{V_\phi}(\theta_n, \phi_n)\mathbf{i}_{\phi_n}], \tag{5}$$

where $u_V(t)$ is the baseband signal of the $V$-port, and $f_0$ represents the carrier frequency. Ignoring the common factor in (5), the coordinate of the $V$-port's electric field vector in the $n$-th antenna's local spherical coordinate system can be simplified as $\tilde{\mathbf{e}}_{V_{n,\mathrm{s}}}(\theta_n, \phi_n) = [G_{V_\theta}(\theta_n, \phi_n), G_{V_\phi}(\theta_n, \phi_n)]^{\mathrm{T}}$.

Consequently, the coordinate of $\mathbf{s}_{V_n}(t)$ in the local Cartesian system of the $n$-th antenna can be calculated by

$$\tilde{\mathbf{e}}_{V_{n,\mathrm{c}}}(\theta_n, \phi_n) = \mathbf{T}_{\mathrm{s2c}}(\theta_n, \phi_n)\tilde{\mathbf{e}}_{V_{n,\mathrm{s}}}(\theta_n, \phi_n) = \begin{bmatrix} \cos\theta_n\cos\phi_n & -\sin\phi_n \\ \cos\theta_n\sin\phi_n & \cos\phi_n \\ -\sin\theta_n & 0 \end{bmatrix} \tilde{\mathbf{e}}_{V_{n,\mathrm{s}}}(\theta_n, \phi_n), \tag{6}$$

where $\mathbf{T}_{\mathrm{s2c}}(\theta_n, \phi_n) \in \mathbb{R}^{3\times 2}$ is the transformation matrix from spherical to Cartesian coordinate system, which is given by the matrix on the right-hand side of the second equality in (6). According to (2) and applying rotation transformation, the coordinate of $\mathbf{s}_{V_n}(t)$ in the global Cartesian coordinate system is given by

$$\mathbf{e}_{V_{n,\mathrm{c}}}(\theta, \phi) = \mathbf{T}_X(-D_n)\mathbf{T}_Y(-E_n)\mathbf{T}_Z(-F_n)\tilde{\mathbf{e}}_{V_{n,\mathrm{c}}}(\theta_n, \phi_n). \tag{7}$$

Hence, in the global spherical coordinate system, the coordinate of $\mathbf{s}_{V_n}(t)$ can be expressed as

$$\mathbf{e}_{V_{n,\mathrm{s}}}(\theta, \phi) = \mathbf{T}_{\mathrm{c2s}}(\theta, \phi)\mathbf{e}_{V_{n,\mathrm{c}}}(\theta, \phi) = \begin{bmatrix} \cos\theta\cos\phi & \cos\theta\sin\phi & -\sin\theta \\ -\sin\phi & \cos\phi & 0 \end{bmatrix} \mathbf{e}_{V_{n,\mathrm{c}}}(\theta, \phi), \tag{8}$$

where $\mathbf{T}_{\mathrm{c2s}}(\theta, \phi) \in \mathbb{R}^{2\times 3}$ denotes the transformation matrix from Cartesian to spherical coordinates, which is given by the matrix on the right-hand side of the second equality in (8). Based on (5) and (8), we transform the electric field of the $V$-port of the $n$-th antenna along $\mathbf{i}_r$ from local to global spherical coordinates. The resulting field vector $\mathbf{e}V_{n,\mathrm{s}}$ has the first element representing the vertical polarization component (global $\theta$-direction) and second element representing the horizontal polarization component (global $\phi$-direction).

Similarly to (5), from the perspective of the local spherical coordinate system, the TEM wave radiated from the $H$-port of the $n$-th antenna at time instant $t$ can be expressed as

$$\mathbf{s}_{H_n}(t) = \sqrt{P_T} u_H(t) \mathrm{e}^{\mathrm{j}2\pi f_0 t} [G_{H_\theta}(\theta_n, \phi_n)\mathbf{i}_{\theta_n} + G_{H_\phi}(\theta_n, \phi_n)\mathbf{i}_{\phi_n}], \tag{9}$$

where $u_H(t)$ is the baseband signal of the $H$-port. In SHV mode, to ensure effective isolation of the pure component at the receiver, signals $u_V(t)$ and $u_H(t)$ are designed as orthogonal baseband waveforms with equal average power $\sigma_s^2$. Ignoring the common factor in (9), the radiated electric field of $H$-port in local spherical coordinate system can be expressed as $\tilde{\mathbf{e}}_{H_{n,\mathrm{s}}}(\theta_n, \phi_n) = [G_{H_\theta}(\theta_n, \phi_n), G_{H_\phi}(\theta_n, \phi_n)]^{\mathrm{T}}$.

Following the same procedure as in (6)–(8), we can transform the electric field of the $H$-port from the local spherical coordinate system to the global spherical coordinate system, denoted as $\mathbf{e}_{H_{n,\mathrm{s}}}(\theta, \phi)$, where the first and second elements represent the vertical and horizontal polarization components, respectively.

In SHV weather radar mode, the $H$- and $V$-channels are activated simultaneously. To accurately calculate meteorological parameters such as the differential reflectivity factor, cross-polarization interference between the two channels needs to be suppressed via transmit beamforming. Taking the $V$-channel as an example, in the global

coordinate system, the $\theta$-direction is the co-polarization direction, while the $\phi$-direction corresponds to the cross-polarization direction. Based on $\mathbf{e}_{V_{n,\mathrm{s}}}(\theta,\phi)$, the co-polarization and cross-polarization beampatterns steering toward $\mathbf{i}_r$ (defined by elevation $\theta$ and azimuth $\phi$) can be respectively expressed as

$$B_{VV_t}(\theta,\phi)=\mathbf{w}_{V_t}^{\mathrm{T}}\mathbf{b}_{VV}(\theta,\phi),\quad B_{VH_t}(\theta,\phi)=\mathbf{w}_{V_t}^{\mathrm{T}}\mathbf{b}_{VH}(\theta,\phi),\tag{10}$$

where $\mathbf{w}_{V_t}=[w_{1,V_t},w_{2,V_t},\ldots,w_{N,V_t}]^{\mathrm{T}}$ is the transmit beamforming weight vector of the $V$-port with $w_{n,V_t}$ being the corresponding complex weight for the $n$-th antenna. $\mathbf{b}_{VV}(\theta,\phi)$ and $\mathbf{b}_{VH}(\theta,\phi)$ are the co-polarization and cross-polarization steering vectors of the $V$-port, respectively, which are defined as

$$\mathbf{b}_{VV}(\theta,\phi)=\left[[\mathbf{e}_{V_{1,\mathrm{s}}}(\theta,\phi)]_1,\ldots,[\mathbf{e}_{V_{N,\mathrm{s}}}(\theta,\phi)]_1\right]^{\mathrm{T}}\odot\mathbf{a}(\theta,\phi),\tag{11}$$

$$\mathbf{b}_{VH}(\theta,\phi)=\left[[\mathbf{e}_{V_{1,\mathrm{s}}}(\theta,\phi)]_2,\ldots,[\mathbf{e}_{V_{N,\mathrm{s}}}(\theta,\phi)]_2\right]^{\mathrm{T}}\odot\mathbf{a}(\theta,\phi),\tag{12}$$

where $\odot$ denotes the element-wise product, and $\mathbf{a}(\theta,\phi)$ is the spatial steering vector towards direction $(\theta,\phi)$ of the conformal array, which is defined as

$$\mathbf{a}(\theta,\phi)=\left[\mathrm{e}^{-\mathrm{j}\frac{2\pi}{\lambda_0}\langle\mathbf{p}_1,\mathbf{i}_r\rangle},\ \mathrm{e}^{-\mathrm{j}\frac{2\pi}{\lambda_0}\langle\mathbf{p}_2,\mathbf{i}_r\rangle},\ldots,\ \mathrm{e}^{-\mathrm{j}\frac{2\pi}{\lambda_0}\langle\mathbf{p}_N,\mathbf{i}_r\rangle}\ \right]^{\mathrm{T}},\tag{13}$$

where $\lambda_0$ is the wavelength, $\mathbf{p}_n$ $(1\leqslant n\leqslant N)$ denotes the position coordinate of the $n$-th antenna in the global Cartesian coordinate system, and $\langle\cdot\rangle$ represents the inner product operation.

For the $H$-channel, the $\phi$-direction is the co-polarization direction and the $\theta$-direction is the cross-polarization direction. Following (10)–(12), the co-polarization and cross-polarization transmit beampatterns are given by

$$B_{HH_t}(\theta,\phi)=\mathbf{w}_{H_t}^{\mathrm{T}}\mathbf{b}_{HH}(\theta,\phi),\quad B_{HV_t}(\theta,\phi)=\mathbf{w}_{H_t}^{\mathrm{T}}\mathbf{b}_{HV}(\theta,\phi),\tag{14}$$

where the co-polarization steering vector $\mathbf{b}_{HH}(\theta,\phi)$ and cross-polarization steering vector $\mathbf{b}_{HV}(\theta,\phi)$ are given by

$$\mathbf{b}_{HH}(\theta,\phi)=\left[[\mathbf{e}_{H_{1,\mathrm{s}}}(\theta,\phi)]_2,\ldots,[\mathbf{e}_{H_{N,\mathrm{s}}}(\theta,\phi)]_2\right]^{\mathrm{T}}\odot\mathbf{a}(\theta,\phi),\tag{15}$$

$$\mathbf{b}_{HV}(\theta,\phi)=\left[[\mathbf{e}_{H_{1,\mathrm{s}}}(\theta,\phi)]_1,\ldots,[\mathbf{e}_{H_{N,\mathrm{s}}}(\theta,\phi)]_1\right]^{\mathrm{T}}\odot\mathbf{a}(\theta,\phi).\tag{16}$$

Based on (10) and (14), in the transmit beamforming design, we optimize the weights for both $V$- and $H$-ports to focus energy along the co-polarization direction toward the target and suppress cross-polarization response. Specifically, we synthesize penciled beampatterns with minimized peak sidelobe levels (PSLLs) for $B_{VV_t}(\theta,\phi)$ and $B_{HH_t}(\theta,\phi)$, while keeping $B_{VH_t}(\theta,\phi)$ and $B_{HV_t}(\theta,\phi)$ as low as possible over the entire observation region.

## 3 Integrated communications and decoding

For the communications function, information is embedded into the radar transmit waveform. By exploiting the additional degrees of freedom (DoFs) offered by polarization, independent communication symbols can be modulated onto different polarization components, thereby increasing the data rate. Assume $K$ downlink users at directions $(\theta_{u_k},\phi_{u_k})$ $(k=1,\ldots,K)$ relative to the transmit array in the global Cartesian coordinate system. According to (5)–(8), for the $n$-th antenna toward the $k$-th user, the $V$- and $H$-port electric fields in global spherical coordinates are $\mathbf{e}_{V_{n,\mathrm{s}}}(\theta_{u_k},\phi_{u_k})$ and $\mathbf{e}_{H_{n,\mathrm{s}}}(\theta_{u_k},\phi_{u_k})$, and in global Cartesian coordinates $\mathbf{e}_{V_{n,\mathrm{c}}}(\theta_{u_k},\phi_{u_k})$ and $\mathbf{e}_{H_{n,\mathrm{c}}}(\theta_{u_k},\phi_{u_k})$.

At the user end, we model the communication receiver with three ideal ports in the global Cartesian coordinate system, corresponding to dipoles aligned along the $X$-, $Y$-, and $Z$-axes. Their radiation beampatterns in the $\theta$- and $\phi$-directions are

$$G_{X_\theta}(\theta,\phi)=l_X\cos\theta\cos\phi,\ G_{X_\phi}(\theta,\phi)=-l_X\sin\phi,\tag{17}$$

$$G_{Y_\theta}(\theta,\phi)=l_Y\cos\theta\sin\phi,\ G_{Y_\phi}(\theta,\phi)=l_Y\cos\phi,\tag{18}$$

$$G_{Z_\theta}(\theta,\phi)=-l_Z\sin\theta,\ G_{Z_\phi}(\theta,\phi)=0,\tag{19}$$

respectively, where the subscripts $X$, $Y$, $Z$ denote the $X$-, $Y$-, and $Z$-ports, and $l_X$, $l_Y$, and $l_Z$ refer to the lengths of the dipoles aligned with the $X$-, $Y$-, and $Z$-axes. Figure 2 provides these six sub-beampatterns for visual illustration.

As for the communication receiver, the incident elevation and azimuth angles of the $k$-th user can be determined from geometric relations as $\pi-\theta_{u_k}$ and $\pi+\phi_{u_k}$, respectively. Substituting these two angles into (1) yields the received

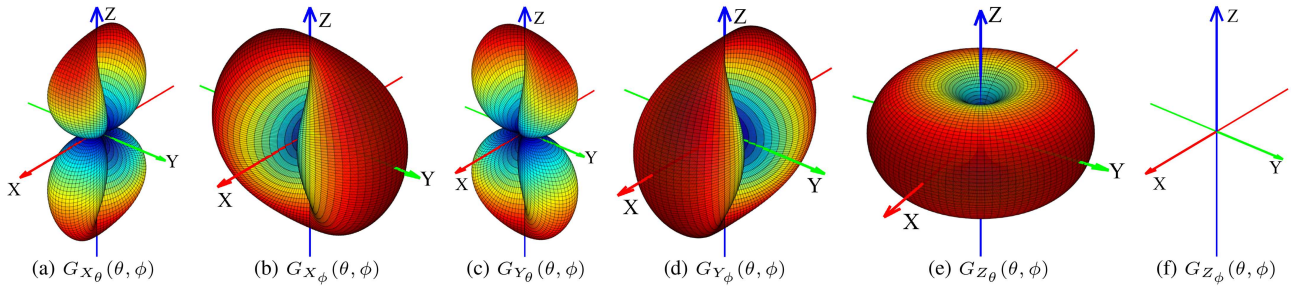


(a) $G_{X_\theta}(\theta,\phi)$ (b) $G_{X_\phi}(\theta,\phi)$ (c) $G_{Y_\theta}(\theta,\phi)$ (d) $G_{Y_\phi}(\theta,\phi)$ (e) $G_{Z_\theta}(\theta,\phi)$ (f) $G_{Z_\phi}(\theta,\phi)$

**Figure 2** (Color online) Sub-beampatterns of an $X$-directed ideal dipole: (a) $\theta$-component; (b) $\phi$-component. $Y$-directed ideal dipole: (c) $\theta$-component; (d) $\phi$-component. $Z$-directed ideal dipole: (e) $\theta$-component; (f) $\phi$-component.

$\theta$- and $\phi$-direction vectors, denoted as $\hat{\mathbf{i}}_{\theta_{u_k}}$ and $\hat{\mathbf{i}}_{\phi_{u_k}}$, which satisfy $\hat{\mathbf{i}}_{\theta_{u_k}}=\mathbf{i}_{\theta_{u_k}}$ and $\hat{\mathbf{i}}_{\phi_{u_k}}=-\mathbf{i}_{\phi_{u_k}}$. Subsequently, taking the $X$-port as an example, the received signal can be expressed as

$$\begin{aligned}y_X(t)=&\beta_{u_k}\sqrt{P_T}(B_{VV_t}(\theta_{u_k},\phi_{u_k})\mathbf{i}_{\theta_{u_k}}+B_{VH_t}(\theta_{u_k},\phi_{u_k})\mathbf{i}_{\phi_{u_k}})^{\mathrm{T}}(G_{X_\theta}(\pi-\theta_{u_k},\pi+\phi_{u_k})\hat{\mathbf{i}}_{\theta_{u_k}}+G_{X_\phi}(\pi-\theta_{u_k},\pi+\phi_{u_k})\hat{\mathbf{i}}_{\phi_{u_k}})\\&u_V(t-\tau_k)\mathrm{e}^{\mathrm{j}2\pi f_{d_k}t}\mathrm{e}^{\mathrm{j}2\pi f_0(t-\tau_k)}+\beta_{u_k}\sqrt{P_T}(B_{HV_t}(\theta_{u_k},\phi_{u_k})\mathbf{i}_{\theta_{u_k}}+B_{HH_t}(\theta_{u_k},\phi_{u_k})\mathbf{i}_{\phi_{u_k}})^{\mathrm{T}}\\&(G_{X_\theta}(\pi-\theta_{u_k},\pi+\phi_{u_k})\hat{\mathbf{i}}_{\theta_{u_k}}+G_{X_\phi}(\pi-\theta_{u_k},\pi+\phi_{u_k})\hat{\mathbf{i}}_{\phi_{u_k}})u_H(t-\tau_k)\mathrm{e}^{\mathrm{j}2\pi f_{d_k}t}\mathrm{e}^{\mathrm{j}2\pi f_0(t-\tau_k)}+n_X(t)\\=&\beta_{u_k}\sqrt{P_T}l_X(B_{VV_t}(\theta_{u_k},\phi_{u_k})\cos\theta_{u_k}\cos\phi_{u_k}-B_{VH_t}(\theta_{u_k},\phi_{u_k})\sin\phi_{u_k})u_V(t-\tau_k)\mathrm{e}^{\mathrm{j}2\pi f_{d_k}t}\mathrm{e}^{\mathrm{j}2\pi f_0(t-\tau_k)}+\\&\beta_{u_k}\sqrt{P_T}l_X(B_{HV_t}(\theta_{u_k},\phi_{u_k})\cos\theta_{u_k}\cos\phi_{u_k}-B_{HH_t}(\theta_{u_k},\phi_{u_k})\sin\phi_{u_k})u_H(t-\tau_k)\mathrm{e}^{\mathrm{j}2\pi f_{d_k}t}\mathrm{e}^{\mathrm{j}2\pi f_0(t-\tau_k)}+n_X(t)\\=&\beta_{u_k}\sqrt{P_t}l_X\left(B_{VX_t}(\theta_{u_k},\phi_{u_k})u_V(t-\tau_k)+B_{HX_t}(\theta_{u_k},\phi_{u_k})u_H(t-\tau_k)\right)\mathrm{e}^{\mathrm{j}2\pi f_{d_k}t}\mathrm{e}^{\mathrm{j}2\pi f_0(t-\tau_k)}+n_X(t),\end{aligned}\tag{20}$$

where $\beta_{u_k}$ denotes the channel coefficient, $f_{d_k}$ represents the doppler shift, $\tau_k$ is the time delay, $n_X(t)$ denotes the noise component, and $B_{VX_t}(\theta_{u_k},\phi_{u_k})$ and $B_{HX_t}(\theta_{u_k},\phi_{u_k})$ are the transmit beampattern components produced by the $V$- and $H$-ports along the $x$-axis, respectively, which are defined as

$$B_{VX_t}(\theta_{u_k},\phi_{u_k})=\mathbf{w}_{V_t}^{\mathrm{T}}\mathbf{b}_{VX}(\theta_{u_k},\phi_{u_k}),\ \mathbf{b}_{VX}(\theta_{u_k},\phi_{u_k})=\left[[\mathbf{e}_{V_{1,\mathrm{c}}}(\theta_{u_k},\phi_{u_k})]_1,\ldots,[\mathbf{e}_{V_{N,\mathrm{c}}}(\theta_{u_k},\phi_{u_k})]_1\right]^{\mathrm{T}}\odot\mathbf{a}(\theta_{u_k},\phi_{u_k}),\tag{21}$$

$$B_{HX_t}(\theta_{u_k},\phi_{u_k})=\mathbf{w}_{H_t}^{\mathrm{T}}\mathbf{b}_{HX}(\theta_{u_k},\phi_{u_k}),\ \mathbf{b}_{HX}(\theta_{u_k},\phi_{u_k})=\left[[\mathbf{e}_{H_{1,\mathrm{c}}}(\theta_{u_k},\phi_{u_k})]_1,\ldots,[\mathbf{e}_{H_{N,\mathrm{c}}}(\theta_{u_k},\phi_{u_k})]_1\right]^{\mathrm{T}}\odot\mathbf{a}(\theta_{u_k},\phi_{u_k}),\tag{22}$$

where $\mathbf{b}_{VX}(\theta_{u_k},\phi_{u_k})$ and $\mathbf{b}_{HX}(\theta_{u_k},\phi_{u_k})$ are the $X$-axis polarization steering vectors for the $k$-th user.

After receiving the signal, the user undergoes down-conversion and conducts matched filtering with $u_V(t)$ and $u_H(t)$, respectively, which yields the outputs as follows:

$$\hat{y}_{VX}=\frac{\mathrm{e}^{\mathrm{j}2\pi f_0\hat{\tau}_k}}{\sigma_s^2\hat{\beta}_{u_k}l_XT}\int_T y_X(t)u_V^*(t-\hat{\tau}_k)\mathrm{e}^{-\mathrm{j}(2\pi\hat{f}_{d_k}t+2\pi f_0t)}\mathrm{d}t,\ \hat{y}_{HX}=\frac{\mathrm{e}^{\mathrm{j}2\pi f_0\hat{\tau}_k}}{\sigma_s^2\hat{\beta}_{u_k}l_XT}\int_T y_X(t)u_H^*(t-\hat{\tau}_k)\mathrm{e}^{-\mathrm{j}(2\pi\hat{f}_{d_k}t+2\pi f_0t)}\mathrm{d}t,\tag{23}$$

where $\hat{\beta}_{u_k}$, $\hat{\tau}_k$, and $\hat{f_{d_k}}$ denote the estimated channel coefficient, Doppler shift, and time delay for the $k$-th user, respectively, which can be accurately obtained via a series of existing strategies [42, 43]. Under the assumption of unbiased estimation, Eq. (23) can be simplified as

$$\hat{y}_{VX}\approx B_{VX_t}(\theta_{u_k},\phi_{u_k})+\hat{n}_{VX},\ \hat{y}_{HX}\approx B_{HX_t}(\theta_{u_k},\phi_{u_k})+\hat{n}_{HX},\tag{24}$$

where $\hat{n}_{VX}$ and $\hat{n}_{HX}$ are the noise component after matched-filtering, given by

$$\hat{n}_{VX}=\frac{\mathrm{e}^{\mathrm{j}2\pi f_0\hat{\tau}_k}}{\sigma_s^2\hat{\beta}_{u_k}l_XT}\int_T n_X(t)u_V^*(t-\hat{\tau}_k)\mathrm{e}^{-\mathrm{j}(2\pi\hat{f}_{d_k}t+2\pi f_0t)}\mathrm{d}t,\hat{n}_{HX}=\frac{\mathrm{e}^{\mathrm{j}2\pi f_0\hat{\tau}_k}}{\sigma_s^2\hat{\beta}_{u_k}l_XT}\int_T n_X(t)u_H^*(t-\hat{\tau}_k)\mathrm{e}^{-\mathrm{j}(2\pi\hat{f}_{d_k}t+2\pi f_0t)}\mathrm{d}t.$$

From (24), the user can decode the $X$-direction beampattern component from the output of the $X$-port. This allows communication information to be embedded into the $X$-direction polarization component at the transmitter. However, embedding independent symbols into $B_{VX_t}(\theta_{u_k},\phi_{u_k})$ or $B_{HX_t}(\theta_{u_k},\phi_{u_k})$ may result in weak radiation in certain directions due to the non-uniform spatial response of the two transmit ports, making reliable communication

difficult. As illustrated in Figure 2, if the $H$-port is equipped with an $X$-dipole, it radiates weakly along the $X$-axis, which hinders communication with users in that direction. To address this, we treat $B_{VX_t}(\theta_{u_k},\phi_{u_k})+B_{HX_t}(\theta_{u_k},\phi_{u_k})$ as a combined communication symbol, embedding information through joint beamforming across both $V$- and $H$-channels. In this way, the complementary radiation characteristics of the two channels can be effectively exploited, such that when one channel has a weak response toward a user direction, the other can provide effective radiation to satisfy the communication requirement. This not only ensures reliable communication information embedding, but also alleviates the additional impact on sensing performance that would otherwise arise from compensating for the weak radiation of an individual channel to satisfy the communication requirement. Accordingly, we define $B_{X_t}(\theta_{u_k},\phi_{u_k})$ as the joint dual-channel $X$-direction transmit beampattern and the joint steering vector $\mathbf{b}_X(\theta_{u_k},\phi_{u_k})=[\mathbf{b}_{VX}^{\mathrm{T}}(\theta_{u_k},\phi_{u_k}),\mathbf{b}_{HX}^{\mathrm{T}}(\theta_{u_k},\phi_{u_k})]^{\mathrm{T}}$. The transmit communication embedding can then be formulated as

$$B_{X_t}(\theta_{u_k},\phi_{u_k})=B_{VX_t}(\theta_{u_k},\phi_{u_k})+B_{HX_t}(\theta_{u_k},\phi_{u_k})=\mathbf{w}_t^{\mathrm{T}}\mathbf{b}_X(\theta_{u_k},\phi_{u_k})=g_{k_X}\mathrm{e}^{\mathrm{j}\psi_{k_X}},\ g_{k_X}\in\mathbb{D}_{\mathrm{A}},\ \psi_{k_X}\in\mathbb{D}_P,\quad(25)$$

where $\mathbf{w}_t=[\mathbf{w}_{V_t}^{\mathrm{T}},\mathbf{w}_{H_t}^{\mathrm{T}}]^{\mathrm{T}}$, and $\mathbb{D}_{\mathrm{A}}$ and $\mathbb{D}_P$ represent the communication dictionaries of amplitude and phase, respectively. At the receive end, the user can decode $B_{VX_t}(\theta_{u_k},\phi_{u_k})$ and $B_{HX_t}(\theta_{u_k},\phi_{u_k})$ separately based on (23) and then compute $B_{X_t}(\theta_{u_k},\phi_{u_k})$.

Analogous to (20)–(25), the received signals at the $Y$- and $Z$-ports are obtained as

$$y_Y(t)=\beta_{u_k}\sqrt{P_T}l_Y\left(B_{VY_t}(\theta_{u_k},\phi_{u_k})u_V(t-\tau_k)+B_{HY_t}(\theta_{u_k},\phi_{u_k})u_H(t-\tau_k)\right)\mathrm{e}^{\mathrm{j}2\pi f_{d_k}t}\mathrm{e}^{\mathrm{j}2\pi f_0(t-\tau_k)}+n_Y(t),\quad(26)$$

$$y_Z(t)=\beta_{u_k}\sqrt{P_T}l_Z\left(B_{VZ_t}(\theta_{u_k},\phi_{u_k})u_V(t-\tau_k)+B_{HZ_t}(\theta_{u_k},\phi_{u_k})u_H(t-\tau_k)\right)\mathrm{e}^{\mathrm{j}2\pi f_{d_k}t}\mathrm{e}^{\mathrm{j}2\pi f_0(t-\tau_k)}+n_Z(t),\quad(27)$$

where $n_Y(t)$ and $n_Z(t)$ are the noise components, $B_{VY_t}(\theta_{u_k},\phi_{u_k})$, $B_{VZ_t}(\theta_{u_k},\phi_{u_k})$, $B_{HY_t}(\theta_{u_k},\phi_{u_k})$, and $B_{HZ_t}(\theta_{u_k},\phi_{u_k})$ are the beampatterns in the $Y$ and $Z$ directions for ports $V$ and $H$, respectively, given by

$$\begin{aligned}&B_{VY_t}(\theta_{u_k},\phi_{u_k})=\mathbf{w}_{V_t}^{\mathrm{T}}\mathbf{b}_{VY}(\theta_{u_k},\phi_{u_k}),\ B_{VZ_t}(\theta_{u_k},\phi_{u_k})=\mathbf{w}_{V_t}^{\mathrm{T}}\mathbf{b}_{VZ}(\theta_{u_k},\phi_{u_k}),\\&B_{HY_t}(\theta_{u_k},\phi_{u_k})=\mathbf{w}_{H_t}^{\mathrm{T}}\mathbf{b}_{HY}(\theta_{u_k},\phi_{u_k}),\ B_{HZ_t}(\theta_{u_k},\phi_{u_k})=\mathbf{w}_{H_t}^{\mathrm{T}}\mathbf{b}_{HZ}(\theta_{u_k},\phi_{u_k}),\end{aligned}\quad(28)$$

with $\mathbf{b}_{VY}(\theta_{u_k},\phi_{u_k})$, $\mathbf{b}_{VZ}(\theta_{u_k},\phi_{u_k})$, $\mathbf{b}_{HY}(\theta_{u_k},\phi_{u_k})$, and $\mathbf{b}_{HZ}(\theta_{u_k},\phi_{u_k})$ being the corresponding polarization steering vectors, which are defined in the same way as $\mathbf{b}_{VX}(\theta_{u_k},\phi_{u_k})$ and $\mathbf{b}_{HX}(\theta_{u_k},\phi_{u_k})$ in (21) and (22).

As shown in (25), we jointly use $B_{VY_t}(\theta_{u_k},\phi_{u_k})$ and $B_{HY_t}(\theta_{u_k},\phi_{u_k})$ to embed communication information along the global $Y$-axis, and jointly use $B_{VZ_t}(\theta_{u_k},\phi_{u_k})$ and $B_{HZ_t}(\theta_{u_k},\phi_{u_k})$ along the $Z$-axis. At the user end, the $Y$-port and $Z$-port decode $B_{VY_t}(\theta_{u_k},\phi_{u_k})+B_{HY_t}(\theta_{u_k},\phi_{u_k})$ and $B_{VZ_t}(\theta_{u_k},\phi_{u_k})+B_{HZ_t}(\theta_{u_k},\phi_{u_k})$ via matched filtering, respectively. Accordingly, the $Y$- and $Z$-direction communication embedding can be expressed as

$$B_{Y_t}(\theta_{u_k},\phi_{u_k})=B_{VY_t}(\theta_{u_k},\phi_{u_k})+B_{HY_t}(\theta_{u_k},\phi_{u_k})=\mathbf{w}_t^{\mathrm{T}}\mathbf{b}_Y(\theta_{u_k},\phi_{u_k})=g_{k_Y}\mathrm{e}^{\mathrm{j}\psi_{k_Y}},\ g_{k_Y}\in\mathbb{D}_{\mathrm{A}},\ \psi_{k_Y}\in\mathbb{D}_P,\quad(29)$$

$$B_{Z_t}(\theta_{u_k},\phi_{u_k})=B_{VZ_t}(\theta_{u_k},\phi_{u_k})+B_{HZ_t}(\theta_{u_k},\phi_{u_k})=\mathbf{w}_t^{\mathrm{T}}\mathbf{b}_Z(\theta_{u_k},\phi_{u_k})=g_{k_Z}\mathrm{e}^{\mathrm{j}\psi_{k_Z}},\ g_{k_Z}\in\mathbb{D}_{\mathrm{A}},\ \psi_{k_Z}\in\mathbb{D}_P,\quad(30)$$

where $\mathbf{b}_Y(\theta_{u_k},\phi_{u_k})=[\mathbf{b}_{VY}^{\mathrm{T}}(\theta_{u_k},\phi_{u_k}),\mathbf{b}_{HY}^{\mathrm{T}}(\theta_{u_k},\phi_{u_k})]^{\mathrm{T}}$ and $\mathbf{b}_Z(\theta_{u_k},\phi_{u_k})=[\mathbf{b}_{VZ}^{\mathrm{T}}(\theta_{u_k},\phi_{u_k}),\mathbf{b}_{HZ}^{\mathrm{T}}(\theta_{u_k},\phi_{u_k})]^{\mathrm{T}}$.

It is worth noting that, compared to conventional beampattern modulation, leveraging polarization characteristics allows communication information to be embedded separately in different polarization components, thereby increasing the communication rate by a factor of three and achieving enhanced communication efficiency.

## 4 Radar receive beamforming

In this section, we develop the receive signal model and beamforming scheme for the polarized conformal weather radar and perform simulations of dual-polarized weather echoes. As illustrated in Figure 1(a), the detection region is divided into $L$ range bins and $P$ angle bins. The received signal comprises not only the desired echo from the target angle bin but also interference from other angle bins. Therefore, the modeling must account for all $P$ angle bins within a given range bin. **Consequently, in this section, the subscript "$p$" (denoting the $p$-th angle bin) is explicitly retained in the expressions for the receive beampatterns and receive weight vectors.**

When scanning the $p$-th angle bin, the transmit main beam is steered toward direction $(\theta_p,\phi_p)$. Based on the

analysis in Section 2, the transmit signal towards direction $(\theta,\phi)$ can be expressed as

$$\mathbf{x}_p(t;\theta,\phi)=\sqrt{P_T}\mathrm{e}^{\mathrm{j}2\pi f_0 t}\left[\mathbf{i}_\theta,\ \mathbf{i}_\phi\right]\begin{bmatrix}B_{VV_t,p}(\theta,\phi)u_V(t)+B_{HV_t,p}(\theta,\phi)u_H(t)\\B_{VH_t,p}(\theta,\phi)u_V(t)+B_{HH_t,p}(\theta,\phi)u_H(t)\end{bmatrix}=\left[\mathbf{i}_\theta,\ \mathbf{i}_\phi\right]\begin{bmatrix}x_{V,p}(t;\theta,\phi)\\x_{H,p}(t;\theta,\phi)\end{bmatrix}. \tag{31}$$

Note that $B_{HV_t,p}(\theta,\phi)$ and $B_{VH_t,p}(\theta,\phi)$ in (31) represent cross-polarization components, which can be suppressed to negligible levels through proper transmit beampattern design.

The signal backscattered from meteorological targets is received by the radar. The received data in the $H$- and $V$-ports for the $s$-th range bin and the $p$-th angle bin can be expressed as

$$\mathbf{y}_{V,s,p}(t;\theta_p,\phi_p)=\sum_{p'=1}^{P}\beta_{s,p'}\left[\mathbf{i}_{\theta_{p'}}\ \mathbf{i}_{\phi_{p'}}\right]\left(\begin{bmatrix}B_{VV_r,p}(\theta_{p'},\phi_{p'})\\B_{VH_r,p}(\theta_{p'},\phi_{p'})\end{bmatrix}\odot\left(\mathbf{\Xi}_{s,p'}\begin{bmatrix}x_{V,p}(t-t_s;\theta_{p'},\phi_{p'})\\x_{H,p}(t-t_s;\theta_{p'},\phi_{p'})\end{bmatrix}\right)\right), \tag{32}$$

$$\mathbf{y}_{H,s,p}(t;\theta_p,\phi_p)=\sum_{p'=1}^{P}\beta_{s,p'}\left[\mathbf{i}_{\theta_{p'}}\ \mathbf{i}_{\phi_{p'}}\right]\left(\begin{bmatrix}B_{HV_r,p}(\theta_{p'},\phi_{p'})\\B_{HH_r,p}(\theta_{p'},\phi_{p'})\end{bmatrix}\odot\left(\mathbf{\Xi}_{s,p'}\begin{bmatrix}x_{V,p}(t-t_s;\theta_{p'},\phi_{p'})\\x_{H,p}(t-t_s;\theta_{p'},\phi_{p'})\end{bmatrix}\right)\right), \tag{33}$$

where $\beta_{s,p'}$ denotes the path loss of the $(s,p')$-th range-angle bin, $\mathbf{\Xi}_{s,p'}=[\xi_{VV,s,p'},\xi_{VH,s,p'};\xi_{HV,s,p'},\xi_{HH,s,p'}]$ is the polarization scattering matrix, whose diagonal and off-diagonal entries represent the co- and cross-polarization scattering coefficients, respectively, and $t_s$ is the transmission delay of the $s$-th range bin. When scanning the $p$-th angle bin, $B_{VV_r,p}(\theta_{p'},\phi_{p'})$ and $B_{VH_r,p}(\theta_{p'},\phi_{p'})$ are the co- and cross-polarization receive beampatterns of the $V$-port, respectively, while $B_{HH_r,p}(\theta_{p'},\phi_{p'})$ and $B_{HV_r,p}(\theta_{p'},\phi_{p'})$ denote those of the $H$-port. Following the definition of the transmit beampatterns given in (10) and (14), the receive beampatterns are defined as

$$\begin{aligned}&B_{VV_r,p}(\theta,\phi)=\mathbf{w}_{V_r,p}^{\mathrm{T}}\mathbf{b}_{VV}(\theta,\phi),\ B_{VH_r,p}(\theta,\phi)=\mathbf{w}_{V_r,p}^{\mathrm{T}}\mathbf{b}_{VH}(\theta,\phi),\\&B_{HH_r,p}(\theta,\phi)=\mathbf{w}_{H_r,p}^{\mathrm{T}}\mathbf{b}_{HH}(\theta,\phi),\ B_{HV_r,p}(\theta,\phi)=\mathbf{w}_{H_r,p}^{\mathrm{T}}\mathbf{b}_{HV}(\theta,\phi),\end{aligned} \tag{34}$$

where $\mathbf{w}_{V_r,p}$ and $\mathbf{w}_{H_r,p}$ are the receive weight vectors for the $V$- and $H$-ports when scanning the $p$-th angle bin.

Accurate estimation of the polarization scattering matrix $\mathbf{\Xi}_{s,p}$ is essential for refined meteorological retrieval, as it fully characterizes precipitation particle scattering under orthogonally polarized waves and provides the basis for extracting key microphysical parameters such as differential reflectivity, differential propagation phase, and copolar correlation coefficient. To achieve high-precision estimation of $\mathbf{\Xi}_{s,p}$, accurately separating the $H$- and $V$-polarization components from the received signals is necessary. This requires receive beampatterns with high gain and good directivity in co-polarization directions, while effectively suppressing cross-polarization components to minimize inter-channel interference. Under SHV mode, the orthogonality between $u_V(t)$ and $u_H(t)$ enables effective separation of their respective components from the coupled received signals in each channel, providing the conditions for accurate estimation of $\mathbf{\Xi}_{s,p}$. Therefore, the receive beamforming aims to synthesize penciled co-polarization beampatterns $B_{VV_r,p}(\theta,\phi)$ and $B_{HH_r,p}(\theta,\phi)$ with low PSLLs, while maintaining low radiation levels for cross-polarization beampatterns $B_{VH_r,p}(\theta,\phi)$ and $B_{HV_r,p}(\theta,\phi)$ across the entire search region.

## 5 Sparse array design for dual-polarized weather radar ISAC

This section presents the design of a sparse dual-polarized phased-array weather radar with integrated communications. Due to payload weight and power constraints on airborne platforms, a sparse array architecture is adopted. Given a fixed aperture, the goal is to minimize the number of antenna elements while jointly optimizing the array layout and beamforming weights to effectively support both sensing and communication functions.

As previously established, meteorological detection requires sequential scanning via both transmit and receive beamforming. On the transmit side (Subsection 2.2), for each angle bin, we synthesize low-PSLL penciled beampatterns in the co-polarization directions of both $H$- and $V$-ports toward the target, while maintaining low cross-polarization levels across the detection region to suppress inter-channel interference. During each scan, communication symbols are simultaneously embedded into the transmit beampatterns directed toward the $K$ downlink users. On the receive side (Section 4), the goal is to similarly synthesize low-PSLL penciled co-polarization beampatterns for each angular bin, while keeping cross-polarization levels low. Notably, although the transmit and receive arrays share the same sparse configuration, their design constraints differ: transmit beamforming typically requires constant-modulus weights due to power amplifier efficiency, whereas receive beamforming does not.

Assume that the joint communication dictionary for all $K$ users over the $X$-, $Y$-, and $Z$-polarization channels is denoted by $\mathbb{D}_c$, containing a total of $Q$ joint symbol combinations. To ensure correct symbol embedding, the transmit weight vectors are specifically designed for each joint symbol combination in $\mathbb{D}_c$ at every scanning angle. **We use subscript "$p,q$" to denote embedding of the $q$-th symbol from $\mathbb{D}_c$ while scanning the $p$-th angle bin, with corresponding transmit weight vectors $\mathbf{w}_{\boldsymbol{V_t,p,q}}$ and $\mathbf{w}_{\boldsymbol{H_t,p,q}}$ for the $V$- and $H$-ports. In contrast, receive beamforming is independent of symbol embedding and tailored solely to the angle bin. Thus, the receive weight vectors are denoted by the single subscript "$p$", i.e., $\mathbf{w}_{\boldsymbol{V_r,p}}$ and $\mathbf{w}_{\boldsymbol{H_r,p}}$.**

Summarizing the above analysis, and using the transmit beampatterns given in (10), (14), the receive beampatterns in (34), and the communication constraints in (25), (29), (30), we can formulate the co-design problem for the sparse dual-polarized phased-array weather radar with integrated communications as

$$\min_{\substack{\mathbf{w}_{V_t,p,q},\mathbf{w}_{H_t,p,q},\\ \mathbf{w}_{V_r,p},\mathbf{w}_{H_r,p},D_{m_t}}} \quad -D_{m_t}+||\mathbf{w}_{V_t,1,1}||_0,\ 1\leqslant p\leqslant P, 1\leqslant q\leqslant Q \tag{35}$$

$$\text{s.t. } \mathbf{w}_{V_t,p,q}^{\mathrm{T}}\mathbf{b}_{VV}(\theta_p,\phi_p)=D_{m_t},\ \mathbf{w}_{H_t,p,q}^{\mathrm{T}}\mathbf{b}_{HH}(\theta_p,\phi_p)=D_{m_t}, \tag{35a}$$

$$|\mathbf{w}_{V_t,p,q}^{\mathrm{T}}\mathbf{b}_{VV}(\theta,\phi)|\leqslant D_{s_t\text{-co}},\ |\mathbf{w}_{H_t,p,q}^{\mathrm{T}}\mathbf{b}_{HH}(\theta,\phi)|\leqslant D_{s_t\text{-co}},\quad (\theta,\phi)\in\boldsymbol{\Theta}_{p,s_t\text{-co}}, \tag{35b}$$

$$|\mathbf{w}_{V_t,p,q}^{\mathrm{T}}\mathbf{b}_{VH}(\theta,\phi)|\leqslant D_{s_t\text{-cr}},\ |\mathbf{w}_{H_t,p,q}^{\mathrm{T}}\mathbf{b}_{HV}(\theta,\phi)|\leqslant D_{s_t\text{-cr}},\quad (\theta,\phi)\in\bar{\boldsymbol{\Theta}}, \tag{35c}$$

$$\mathbf{w}_{V_r,p}^{\mathrm{T}}\mathbf{b}_{VV}(\theta_p,\phi_p)=D_{m_r},\ \mathbf{w}_{H_r,p}^{\mathrm{T}}\mathbf{b}_{HH}(\theta_p,\phi_p)=D_{m_r}, \tag{35d}$$

$$|\mathbf{w}_{V_r,p}^{\mathrm{T}}\mathbf{b}_{VV}(\theta,\phi)|\leqslant D_{s_r\text{-co}},\ |\mathbf{w}_{H_r,p}^{\mathrm{T}}\mathbf{b}_{HH}(\theta,\phi)|\leqslant D_{s_r\text{-co}},\quad (\theta,\phi)\in\boldsymbol{\Theta}_{p,s_r\text{-co}}, \tag{35e}$$

$$|\mathbf{w}_{V_r,p}^{\mathrm{T}}\mathbf{b}_{VH}(\theta,\phi)|\leqslant D_{s_r\text{-cr}},\ |\mathbf{w}_{H_r,p}^{\mathrm{T}}\mathbf{b}_{HV}(\theta,\phi)|\leqslant D_{s_r\text{-cr}},\quad (\theta,\phi)\in\bar{\boldsymbol{\Theta}}, \tag{35f}$$

$$\mathbf{w}_{t,p,q}^{\mathrm{T}}\mathbf{B}_c=\mathbf{c}_q^{\mathrm{T}},\mathbf{w}_{t,p,q}=[\mathbf{w}_{V_t,p,q}^{\mathrm{T}},\mathbf{w}_{H_t,p,q}^{\mathrm{T}}]^{\mathrm{T}}, \tag{35g}$$

$$\mathbf{S}(\mathbf{w}_{V_t,p,q})=\mathbf{S}(\mathbf{w}_{H_t,p,q})=\mathbf{S}(\mathbf{w}_{V_r,p})=\mathbf{S}(\mathbf{w}_{H_r,p}), \tag{35h}$$

$$|\mathbf{w}_{V_t,p,q}[n]|\in\{0,1\},\ |\mathbf{w}_{H_t,p,q}[n]|\in\{0,1\},\ n=1,\ldots,N, \tag{35i}$$

where $||.||_0$ denotes the $l_0$-norm, and $\mathbf{c}_q=[c_{q,1}^X,c_{q,1}^Y,c_{q,1}^Z,\ldots,c_{q,K}^X,c_{q,K}^Y,c_{q,K}^Z]^{\mathrm{T}}$ denotes the $q$-th joint communication symbol vector in $\mathbb{D}_c$, with $c_{q,k}^X$, $c_{q,k}^Y$, and $c_{q,k}^Z$ representing the symbols embedded into the $X$-, $Y$-, and $Z$-polarization channels of the $k$-th user, respectively. Constraints (35a)–(35c) govern transmit beamforming, where $D_{m_t}\in\mathbb{R}$ and $D_{s_t\text{-co}}\in\mathbb{R}$ specify the mainlobe gain and PSLL, respectively. $\bar{\boldsymbol{\Theta}}$ denotes the entire angular region considered for beampattern synthesis, while $\boldsymbol{\Theta}_{p,s_t\text{-co}}$ denotes the co-polarization sidelobe region for the $p$-th scan, obtained by excluding the corresponding mainlobe region and the communication-user protection intervals from $\bar{\boldsymbol{\Theta}}$. $D_{s_t\text{-cr}}\in\mathbb{R}$ specifies the cross-polarization radiation threshold over $\bar{\boldsymbol{\Theta}}$. Constraints (35d)–(35f) similarly define receive beamforming requirements, with $D_{m_r}\in\mathbb{R}$, $D_{s_r\text{-co}}\in\mathbb{R}$ and $\boldsymbol{\Theta}_{p,s_r\text{-co}}$, and $D_{s_r\text{-cr}}\in\mathbb{R}$ as the corresponding metrics for receive beampatterns.

It should be noted that for (35a) and (35d), the mainlobe gains of the $H$- and $V$-channel co-polarization beampatterns are required to be real and equal to ensure orthogonality between the two channels, facilitating signal separation and accurate scattering matrix estimation. Without loss of generality, $D_{m_r}$ can be set to "1". Constraint (35g) specifies the communication embedding requirement, where

$$\mathbf{B}_c=[\mathbf{b}_X(\theta_{u_1},\phi_{u_1}),\mathbf{b}_Y(\theta_{u_1},\phi_{u_1}),\mathbf{b}_Z(\theta_{u_1},\phi_{u_1}),\ldots,\mathbf{b}_X(\theta_{u_K},\phi_{u_K}),\mathbf{b}_Y(\theta_{u_K},\phi_{u_K}),\mathbf{b}_Z(\theta_{u_K},\phi_{u_K})].$$

Besides, constraint (35h) enforces a common sparse structure for both polarizations across all transmit and receive weights over all $p$ and $q$, and (35i) imposes the constant modulus requirement on the transmit weights.

To facilitate the subsequent optimization, we reformulate the constraints in (35) into compact matrix forms with respect to the aggregated transmit and receive beamforming variables. Specifically, the mainlobe, sidelobe/cross-polarization, communication, and sparsity constraints are handled successively below.

The transmit co-polarization mainlobe constraint (35a) can be reformulated as

$$\check{\mathbf{B}}_{m_t}^{\mathrm{T}}\check{\mathbf{w}}_t=\check{\mathbf{d}}_{m_t}, \tag{36}$$

where $\check{\mathbf{w}}_t=\left[[\mathbf{w}_{t,1,1}^{\mathrm{T}},\ldots,\mathbf{w}_{t,P,1}^{\mathrm{T}}],[\mathbf{w}_{t,1,2}^{\mathrm{T}},\ldots,\mathbf{w}_{t,P,2}^{\mathrm{T}}],\ldots,[\mathbf{w}_{t,1,Q}^{\mathrm{T}},\ldots,\mathbf{w}_{t,P,Q}^{\mathrm{T}}]\right]^{\mathrm{T}}$, $\check{\mathbf{d}}_{m_t}=D_{m_t}\mathbf{1}_{2PQ}$, and

$$\check{\mathbf{B}}_{m_t}=\mathbf{I}_Q\otimes\mathrm{blkdiag}\left(\mathbf{B}_{m_t,1},\ldots,\mathbf{B}_{m_t,P}\right),\mathbf{B}_{m_t,p}=\mathrm{blkdiag}\left(\mathbf{b}_{VV}(\theta_p,\phi_p),\mathbf{b}_{HH}(\theta_p,\phi_p)\right).$$

The receive co-polarization mainlobe constraint (35d) can be transformed into

$$\check{\mathbf{B}}_{m_r}^{\mathrm{T}}\check{\mathbf{w}}_r=\check{\mathbf{d}}_{m_r}, \tag{37}$$

where $\check{\mathbf{w}}_r=\left[\mathbf{w}_{r,1}^{\mathrm{T}},\ldots,\mathbf{w}_{r,P}^{\mathrm{T}}\right]^{\mathrm{T}}$, $\mathbf{w}_{r,p}=[\mathbf{w}_{V_r,p}^{\mathrm{T}},\mathbf{w}_{H_r,p}^{\mathrm{T}}]^{\mathrm{T}}$, $\check{\mathbf{d}}_{m_r}=D_{m_r}\mathbf{1}_{2P}$, and $\check{\mathbf{B}}_{m_r}=\mathrm{blkdiag}\left(\mathbf{B}_{m_t,1},\ldots,\mathbf{B}_{m_t,P}\right)$.

The transmit co-polarization sidelobe and cross-polarization constraints (35b) and (35c) can be rewritten as

$$|\check{\mathbf{B}}_{s_t}^{\mathrm{T}}\check{\mathbf{w}}_t|\preceq\check{\mathbf{d}}_{s_t}, \tag{38}$$

where "$\preceq$" indicates that each entry of the left-hand side (LHS) vector is no more than the corresponding entry of the right-hand side (RHS) vector

$$\begin{aligned}
&\check{\mathbf{B}}_{s_t}=[\check{\mathbf{B}}_{s_t\text{-co}},\check{\mathbf{B}}_{t\text{-cr}}],\ \check{\mathbf{B}}_{s_t\text{-co}}=\mathbf{I}_Q\otimes\mathrm{blkdiag}\left(\mathbf{B}_{1,s_t\text{-co}},\ldots,\mathbf{B}_{P,s_t\text{-co}}\right),\ \check{\mathbf{B}}_{t\text{-cr}}=\mathbf{I}_Q\otimes\mathbf{I}_P\otimes\mathbf{B}_{\mathrm{cr}},\\
&\mathbf{B}_{p,s_t\text{-co}}=\mathrm{blkdiag}\left(\mathbf{B}_{p,V_t\text{-co}},\mathbf{B}_{p,H_t\text{-co}}\right),\mathbf{B}_{p,V_t\text{-co}}=[\mathbf{b}_{VV}(\theta_{t_{\mathrm{co}},p,1},\phi_{t_{\mathrm{co}},p,1}),\ldots,\mathbf{b}_{VV}(\theta_{t_{\mathrm{co}},p,S_{t,p}},\phi_{t_{\mathrm{co}},p,S_{t,p}})],\\
&\mathbf{B}_{p,H_t\text{-co}}=[\mathbf{b}_{HH}(\theta_{t_{\mathrm{co}},p,1},\phi_{t_{\mathrm{co}},p,1}),\ldots,\mathbf{b}_{HH}(\theta_{t_{\mathrm{co}},p,S_{t,p}},\phi_{t_{\mathrm{co}},p,S_{t,p}})],\mathbf{B}_{\mathrm{cr}}=\mathrm{blkdiag}\left(\mathbf{B}_{V\text{-cr}},\mathbf{B}_{H\text{-cr}}\right),\\
&\mathbf{B}_{V\text{-cr}}=[\mathbf{b}_{VH}(\theta_{\mathrm{cr},1},\phi_{\mathrm{cr},1}),\ldots,\mathbf{b}_{VH}(\theta_{\mathrm{cr},S},\phi_{\mathrm{cr},S})],\mathbf{B}_{H\text{-cr}}=[\mathbf{b}_{HV}(\theta_{\mathrm{cr},1},\phi_{\mathrm{cr},1}),\ldots,\mathbf{b}_{HV}(\theta_{\mathrm{cr},S},\phi_{\mathrm{cr},S})],
\end{aligned}$$

$\check{\mathbf{d}}_{s_t}=[D_{s_t\text{-co}}\mathbf{1}_{\check{S}_{t\text{-co}}}^{\mathrm{T}},D_{s_t\text{-cr}}\mathbf{1}_{\check{S}_{t\text{-cr}}}^{\mathrm{T}}]^{\mathrm{T}}$, $(\theta_{t_{\mathrm{co}},p,i},\phi_{t_{\mathrm{co}},p,i})$ and $(\theta_{\mathrm{cr},i},\phi_{\mathrm{cr},i})$ represent the $i$-th elements of sets $\boldsymbol{\Theta}_{p,s_t\text{-co}}$ and $\bar{\boldsymbol{\Theta}}$, respectively, $S_{t,p}$ and $S$ are the cardinalities of the two sets, $\check{S}_{t\text{-co}}=2Q\times(\sum_{p=1}^{P}S_{t,p})$, and $\check{S}_{t\text{-cr}}=2PQS$. Similarly, the receive co-polarization sidelobe and cross-polarization constraints (35e) and (35f) can be rewritten as

$$|\check{\mathbf{B}}_{s_r}^{\mathrm{T}}\check{\mathbf{w}}_r|\preceq\check{\mathbf{d}}_{s_r}, \tag{39}$$

where $\check{\mathbf{d}}_{s_r}=[D_{s_r\text{-co}}\mathbf{1}_{\check{S}_{r\text{-co}}}^{\mathrm{T}},D_{s_r\text{-cr}}\mathbf{1}_{\check{S}_{r\text{-cr}}}^{\mathrm{T}}]^{\mathrm{T}}$, $\check{S}_{r\text{-co}}=\sum_{p=1}^{P}2S_{r,p}$, $\check{S}_{r\text{-cr}}=2PS$, $S_{r,p}$ denotes the cardinality of $\boldsymbol{\Theta}_{p,s_r\text{-co}}$,

$$\begin{aligned}
&\check{\mathbf{B}}_{s_r}=[\check{\mathbf{B}}_{s_r\text{-co}},\check{\mathbf{B}}_{r\text{-cr}}],\ \check{\mathbf{B}}_{s_r\text{-co}}=\mathrm{blkdiag}\left(\mathbf{B}_{1,s_r\text{-co}},\ldots,\mathbf{B}_{P,s_r\text{-co}}\right),\ \check{\mathbf{B}}_{r\text{-cr}}=\mathbf{I}_P\otimes\mathbf{B}_{\mathrm{cr}},\\
&\mathbf{B}_{p,s_r\text{-co}}=\mathrm{blkdiag}\left(\mathbf{B}_{p,V_r\text{-co}},\ \mathbf{B}_{p,H_r\text{-co}}\right),\mathbf{B}_{p,V_r\text{-co}}=[\mathbf{b}_{VV}(\theta_{r_{\mathrm{co}},p,1},\phi_{r_{\mathrm{co}},p,1}),\ldots,\mathbf{b}_{VV}(\theta_{r_{\mathrm{co}},p,S_{r,p}},\phi_{r_{\mathrm{co}},p,S_{r,p}})],\\
&\mathbf{B}_{p,H_r\text{-co}}=[\mathbf{b}_{HH}(\theta_{r_{\mathrm{co}},p,1},\phi_{r_{\mathrm{co}},p,1}),\ldots,\mathbf{b}_{HH}(\theta_{r_{\mathrm{co}},p,S_{r,p}},\phi_{r_{\mathrm{co}},p,S_{r,p}})],
\end{aligned}$$

and $(\theta_{r_{\mathrm{co}},p,i},\phi_{r_{\mathrm{co}},p,i})$ represents the $i$-th elements of set $\boldsymbol{\Theta}_{p,s_r\text{-co}}$.

Since the transmit and receive sidelobe/cross-polarization constraints have the same element-wise inequality form, Eqs. (38) and (39) can be stacked into the following unified constraint

$$|\check{\mathbf{B}}_s^{\mathrm{T}}\check{\mathbf{w}}|\preceq\check{\mathbf{d}}_s, \tag{40}$$

where $\check{\mathbf{B}}_s=\mathrm{blkdiag}(\check{\mathbf{B}}_{s_t},\check{\mathbf{B}}_{s_r})$, $\check{\mathbf{w}}=[\check{\mathbf{w}}_t^{\mathrm{T}},\check{\mathbf{w}}_r^{\mathrm{T}}]^{\mathrm{T}}$, and $\check{\mathbf{d}}_s=[\check{\mathbf{d}}_{s_t}^{\mathrm{T}},\check{\mathbf{d}}_{s_r}^{\mathrm{T}}]^{\mathrm{T}}$.

In terms of the communication constraint (35g), it can be reorganized as

$$\check{\mathbf{B}}_c^{\mathrm{T}}\check{\mathbf{w}}_t=\check{\mathbf{g}}_c, \tag{41}$$

where $\check{\mathbf{g}}_c=[\mathbf{1}_P^{\mathrm{T}}\otimes\mathbf{c}_1^{\mathrm{T}},\ldots,\mathbf{1}_P^{\mathrm{T}}\otimes\mathbf{c}_Q^{\mathrm{T}}]^{\mathrm{T}}$ and $\check{\mathbf{B}}_c=\mathbf{I}_{PQ}\otimes\mathbf{B}_c$. Furthermore, from the perspective of $\check{\mathbf{w}}$, the $l_0$-norm in the objective function of (35) and the sparsity constraint (35h) are equivalent to the following formulation:

$$\min_{\check{\mathbf{w}},\mathbf{z}}\ ||\mathbf{z}||_0 \tag{42}$$

$$\text{s.t.}\ \left\|\left(\mathbf{I}_{2(PQ+P)}\otimes\mathbf{e}_n\right)^{\mathrm{T}}\check{\mathbf{w}}\right\|_2^2\leqslant\mathbf{z}[n],\ n=1,\ldots,N, \tag{42a}$$

where $\mathbf{e}_n=[\underbrace{0,\ldots,0}_{n-1\ \text{"0"s}},1,\underbrace{0,\ldots,0}_{N-n\ \text{"0"s}}]^{\mathrm{T}}$ is the antenna selection vector.

Summarizing (36), (37), (40)–(42), problem (35) can be equivalently reformulated in terms of the variable $\check{\mathbf{w}}$ as follows:

$$\begin{aligned}
(\mathcal{P})\quad &\min_{\check{\mathbf{w}},\mathbf{z},D_{m_t}}\ -D_{m_t}+\|\mathbf{z}\|_0\\
&\text{s.t.}\quad (36),(37),(40),(41),(42\text{a}),
\end{aligned} \tag{43}$$

$$|\check{\mathbf{w}}_t[i]| \in \{0,1\},\ i=1,\ldots,2NPQ. \tag{43a}$$

Problem $(\mathcal{P})$ is non-convex due to the $l_0$-norm in the objective function and constraints (42a) and (43a), making direct optimization intractable. To address this, we adopt the ADMM. ADMM has been widely adopted for ISAC and sparse array optimization problems with similar coupled structures [29,50–52]. The considered problem contains highly coupled sparsity, constant modulus, and sensing/communication constraints. By exploiting variable splitting, ADMM can decompose these coupled components into several structured subproblems and is therefore well suited to the considered formulation.

By introducing auxiliary variables $\check{\mathbf{y}}_t=\check{\mathbf{w}}_t$ and $\check{\mathbf{u}}_s=\check{\mathbf{B}}_s^{\mathrm{T}}\check{\mathbf{w}}$, we reformulate $(\mathcal{P})$ as

$$\begin{aligned}
(\mathcal{P}') \quad \min_{\check{\mathbf{w}},\mathbf{z},\check{\mathbf{y}}_t,\check{\mathbf{u}}_s,D_{m_t}} \ & -D_{m_t}+||\mathbf{z}||_0 && (44)\\
\text{s.t. } & \check{\mathbf{B}}_{m_t}^{\mathrm{T}}\check{\mathbf{w}}_t=D_{m_t}\mathbf{1}_{2PQ}, && (44a)\\
& \check{\mathbf{B}}_{m_r}^{\mathrm{T}}\check{\mathbf{w}}_r=\check{\mathbf{d}}_{m_r}, && (44b)\\
& |\check{\mathbf{u}}_s|\preceq\check{\mathbf{d}}_s, && (44c)\\
& \check{\mathbf{B}}_c^{\mathrm{T}}\check{\mathbf{w}}_t=\check{\mathbf{g}}_c, && (44d)\\
& \left\|\left(\mathbf{I}_{2(PQ+P)}\otimes\mathbf{e}_n\right)^{\mathrm{T}}\check{\mathbf{w}}\right\|_2^2\leqslant\mathbf{z}[n],\ n=1,\ldots,N, && (44e)\\
& |\check{\mathbf{y}}_t[i]|\in\{0,1\},\ i=1,\ldots,2NPQ, && (44f)\\
& \check{\mathbf{y}}_t=\check{\mathbf{w}}_t,\ \check{\mathbf{u}}_s=\check{\mathbf{B}}_s^{\mathrm{T}}\check{\mathbf{w}}. && (44g)
\end{aligned}$$

Based on the objective and equality constraints of $(\mathcal{P}')$, we formulate the augmented Lagrangian function as

$$\begin{aligned}
&\mathcal{L}(\check{\mathbf{w}},\mathbf{z},\check{\mathbf{y}}_t,\check{\mathbf{u}}_s,D_{m_t},\check{\boldsymbol{\lambda}}_t,\check{\mathbf{v}}_{m_t},\check{\mathbf{v}}_{m_r},\check{\mathbf{v}}_s,\check{\mathbf{v}}_c)=-D_{m_t}+||\mathbf{z}||_0+\frac{\rho_1}{2}\left(||\check{\mathbf{y}}_t-\check{\mathbf{w}}_t+\check{\boldsymbol{\lambda}}_t||_2^2-||\check{\boldsymbol{\lambda}}_t||_2^2\right) \\
&+\frac{\rho_2}{2}\left(||D_{m_t}\mathbf{1}_{2PQ}-\check{\mathbf{B}}_{m_t}^{\mathrm{T}}\check{\mathbf{w}}_t+\check{\mathbf{v}}_{m_t}||_2^2-||\check{\mathbf{v}}_{m_t}||_2^2\right)+\frac{\rho_3}{2}\left(||\check{\mathbf{d}}_{m_r}-\check{\mathbf{B}}_{m_r}^{\mathrm{T}}\check{\mathbf{w}}_r+\check{\mathbf{v}}_{m_r}||_2^2-||\check{\mathbf{v}}_{m_r}||_2^2\right) \\
&+\frac{\rho_4}{2}\left(||\check{\mathbf{u}}_s-\check{\mathbf{B}}_s^{\mathrm{T}}\check{\mathbf{w}}+\check{\mathbf{v}}_s||_2^2-||\check{\mathbf{v}}_s||_2^2\right)+\frac{\rho_5}{2}\left(||\check{\mathbf{g}}_c-\check{\mathbf{B}}_c^{\mathrm{T}}\check{\mathbf{w}}_t+\check{\mathbf{v}}_c||_2^2-||\check{\mathbf{v}}_c||_2^2\right),
\end{aligned} \tag{45}$$

where $\rho_i$ $(i=1,\ldots,5)$ are penalty parameters, and $\check{\boldsymbol{\lambda}}_t$, $\check{\mathbf{v}}_{m_t}$, $\check{\mathbf{v}}_{m_r}$, $\check{\mathbf{v}}_s$, and $\check{\mathbf{v}}_c$ are scaled dual variables. Under the framework of the ADMM, the original problem can be decomposed into subproblems with respect to each variable, which are then solved via alternating optimization. The specific steps for the $(l+1)$-th iteration are as follows:

$$\begin{cases}
(\mathcal{P}_1) & \check{\mathbf{u}}_s^{(l+1)}=\underset{\check{\mathbf{u}}_s}{\operatorname{argmin}}\ \mathcal{L}\left(\check{\mathbf{w}}^{(l)},\mathbf{z}^{(l)},\check{\mathbf{y}}_t^{(l)},\check{\mathbf{u}}_s,D_{m_t}^{(l)},\check{\boldsymbol{\lambda}}_t^{(l)},\check{\mathbf{v}}_{m_t}^{(l)},\check{\mathbf{v}}_{m_r}^{(l)},\check{\mathbf{v}}_s^{(l)},\check{\mathbf{v}}_c^{(l)}\right),\ \text{s.t. (44c)},\\
(\mathcal{P}_2) & \check{\mathbf{y}}_t^{(l+1)}=\underset{\check{\mathbf{y}}_t}{\operatorname{argmin}}\ \mathcal{L}\left(\check{\mathbf{w}}^{(l)},\mathbf{z}^{(l)},\check{\mathbf{y}}_t,\check{\mathbf{u}}_s^{(l+1)},D_{m_t}^{(l)},\check{\boldsymbol{\lambda}}_t^{(l)},\check{\mathbf{v}}_{m_t}^{(l)},\check{\mathbf{v}}_{m_r}^{(l)},\check{\mathbf{v}}_s^{(l)},\check{\mathbf{v}}_c^{(l)}\right),\ \text{s.t. (44f)},\\
(\mathcal{P}_3) & (\check{\mathbf{w}}^{(l+1)},\mathbf{z}^{(l+1)})=\underset{\check{\mathbf{w}},\mathbf{z}}{\operatorname{argmin}}\ \mathcal{L}\left(\check{\mathbf{w}},\mathbf{z},\check{\mathbf{y}}_t^{(l+1)},\check{\mathbf{u}}_s^{(l+1)},D_{m_t}^{(l)},\check{\boldsymbol{\lambda}}_t^{(l)},\check{\mathbf{v}}_{m_t}^{(l)},\check{\mathbf{v}}_{m_r}^{(l)},\check{\mathbf{v}}_s^{(l)},\check{\mathbf{v}}_c^{(l)}\right),\ \text{s.t. (44e)},\\
(\mathcal{P}_4) & D_{m_t}^{(l+1)}=\underset{D_{m_t}}{\operatorname{argmin}}\ \mathcal{L}\left(\check{\mathbf{w}}^{(l+1)},\mathbf{z}^{(l+1)},\check{\mathbf{y}}_t^{(l+1)},\check{\mathbf{u}}_s^{(l+1)},D_{m_t},\check{\boldsymbol{\lambda}}_t^{(l)},\check{\mathbf{v}}_{m_t}^{(l)},\check{\mathbf{v}}_{m_r}^{(l)},\check{\mathbf{v}}_s^{(l)},\check{\mathbf{v}}_c^{(l)}\right),\\
(\mathcal{P}_5) & \check{\boldsymbol{\lambda}}_t^{(l+1)}=\check{\boldsymbol{\lambda}}_t^{(l)}+\check{\mathbf{y}}_t^{(l+1)}-\check{\mathbf{w}}_t^{(l+1)},\check{\mathbf{v}}_s^{(l+1)}=\check{\mathbf{v}}_s^{(l)}+\check{\mathbf{u}}_s^{(l+1)}-\check{\mathbf{B}}_s^{\mathrm{T}}\check{\mathbf{w}}^{(l+1)},\check{\mathbf{v}}_c^{(l+1)}=\check{\mathbf{v}}_c^{(l)}+\check{\mathbf{g}}_c-\check{\mathbf{B}}_c^{\mathrm{T}}\check{\mathbf{w}}_t^{(l+1)},\\
& \check{\mathbf{v}}_{m_r}^{(l+1)}=\check{\mathbf{v}}_{m_r}^{(l)}+\check{\mathbf{d}}_{m_r}-\check{\mathbf{B}}_{m_r}^{\mathrm{T}}\check{\mathbf{w}}_r^{(l+1)},\check{\mathbf{v}}_{m_t}^{(l+1)}=\check{\mathbf{v}}_{m_t}^{(l)}+D_{m_t}^{(l+1)}\mathbf{1}_{2PQ}-\check{\mathbf{B}}_{m_t}^{\mathrm{T}}\check{\mathbf{w}}_t^{(l+1)}.
\end{cases} \tag{46}$$

In the following, we derive the closed-form solutions for each subproblem in (46) respectively.

### 5.1 Solution to $(\mathcal{P}_1)$

By ignoring the constant terms in the objective function, $(\mathcal{P}_1)$ can be reformulated as follows:

$$(\mathcal{P}_1)\quad \min_{\check{\mathbf{u}}_s}\ ||\check{\mathbf{u}}_s-\check{\mathbf{B}}_s^{\mathrm{T}}\check{\mathbf{w}}^{(l)}+\check{\mathbf{v}}_s^{(l)}||_2^2\quad\text{s.t. (44c)}. \tag{47}$$

It can be observed from (47) that the optimization with respect to each element of $\check{\mathbf{u}}_s$ in $(\mathcal{P}_1)$ is independent, and thus they can be optimized separately. For the $i$-th element of $\check{\mathbf{u}}_s$, the optimization problem is given by

$$(\mathcal{P}_{1-1}) \quad \min_{\check{\mathbf{u}}_s[i]} |\check{\mathbf{u}}_s[i] - [\check{\mathbf{B}}_s]_i^{\mathrm{T}} \check{\mathbf{w}}^{(l)} + \check{\mathbf{v}}_s^{(l)}[i]|_2^2 \tag{48}$$

$$\text{s.t. } |\check{\mathbf{u}}_s[i]| \leqslant \check{\mathbf{d}}_s[i]. \tag{48a}$$

Hence, the closed-form solution for updating $\check{\mathbf{u}}_s$ can be expressed as

$$\check{\mathbf{u}}_s^{(l+1)}[i] = \begin{cases} [\check{\mathbf{B}}_s]_i^{\mathrm{T}} \check{\mathbf{w}}^{(l)} - \check{\mathbf{v}}_s^{(l)}[i], & \text{if } |[\check{\mathbf{B}}_s]_i^{\mathrm{T}} \check{\mathbf{w}}^{(l)} - \check{\mathbf{v}}_s^{(l)}[i]| \leqslant \check{\mathbf{d}}_s[i], \\ \check{\mathbf{d}}_s[i] \mathrm{e}^{\mathrm{j}\angle([\check{\mathbf{B}}_s]_i^{\mathrm{T}} \check{\mathbf{w}}^{(l)} - \check{\mathbf{v}}_s^{(l)}[i])}, & \text{if } |[\check{\mathbf{B}}_s]_i^{\mathrm{T}} \check{\mathbf{w}}^{(l)} - \check{\mathbf{v}}_s^{(l)}[i]| > \check{\mathbf{d}}_s[i]. \end{cases} \tag{49}$$

### 5.2 Solution to $(\mathcal{P}_2)$

Omitting the terms independent of $\check{\mathbf{y}}_t$ in $(\mathcal{P}_2)$, the optimization problem with respect to $\check{\mathbf{y}}_t$ can be expressed as

$$(\mathcal{P}_2) \quad \min_{\check{\mathbf{y}}_t} ||\check{\mathbf{y}}_t - \check{\mathbf{w}}_t^{(l)} + \check{\boldsymbol{\lambda}}_t^{(l)}||_2^2 \quad \text{s.t. (44f).} \tag{50}$$

Likewise, the optimization in $(\mathcal{P}_2)$ can be performed element by element, which leads to the following formulation:

$$(\mathcal{P}_{2-1}) \quad \min_{\check{\mathbf{y}}_t[i]} |\check{\mathbf{y}}_t[i] - \check{\mathbf{w}}_t^{(l)}[i] + \check{\boldsymbol{\lambda}}_t^{(l)}[i]|_2^2 \quad \text{s.t. } |\check{\mathbf{y}}_t[i]| \in \{0, 1\}. \tag{51}$$

And the solution to $(\mathcal{P}_{2-1})$ is given by

$$\check{\mathbf{y}}_t^{(l+1)}[i] = \begin{cases} \mathrm{e}^{\mathrm{j}\angle(\check{\mathbf{w}}_t^{(l)}[i] - \check{\boldsymbol{\lambda}}_t^{(l)}[i])}, & \text{if } |\check{\mathbf{w}}_t^{(l)}[i] - \check{\boldsymbol{\lambda}}_t^{(l)}[i]| \geqslant \frac{1}{2}, \\ 0, & \text{if } |\check{\mathbf{w}}_t^{(l)}[i] - \check{\boldsymbol{\lambda}}_t^{(l)}[i]| < \frac{1}{2}. \end{cases} \tag{52}$$

### 5.3 Solution to $(\mathcal{P}_3)$

Following the update of $\check{\mathbf{u}}_s$ and $\check{\mathbf{y}}_t$, we then optimize $\check{\mathbf{w}}$ and $\mathbf{z}$ by reformulating $(\mathcal{P}_3)$ as

$$(\mathcal{P}_3) \quad \min_{\check{\mathbf{w}}, \mathbf{z}} \mathcal{L}(\check{\mathbf{w}}, \mathbf{z}, \check{\mathbf{y}}_t^{(l+1)}, \check{\mathbf{u}}_s^{(l+1)}, D_{m_t}^{(l)}, \check{\boldsymbol{\lambda}}_t^{(l)}, \check{\mathbf{v}}_{m_t}^{(l)}, \check{\mathbf{v}}_{m_r}^{(l)}, \check{\mathbf{v}}_s^{(l)}, \check{\mathbf{v}}_c^{(l)}) \quad \text{s.t. (44e).} \tag{53}$$

Ignoring the constant term in the objective function, $(\mathcal{P}_3)$ can be simplified to

$$(\mathcal{P}_3') \quad \min_{\mathbf{z}, \check{\mathbf{w}}} ||\mathbf{z}||_0 + ||\check{\mathbf{h}} - \check{\mathbf{B}}\check{\mathbf{w}}||_2^2 \quad \text{s.t. (44e)}, \tag{54}$$

where

$$\check{\mathbf{h}} = \begin{bmatrix} \sqrt{\rho_1/2}(\check{\mathbf{y}}_t^{(l+1)} + \check{\boldsymbol{\lambda}}_t^{(l)}) \\ \sqrt{\rho_2/2}(D_{m_t}^{(l)} \mathbf{1}_{2PQ} + \check{\mathbf{v}}_{m_t}^{(l)}) \\ \sqrt{\rho_3/2}(\check{\mathbf{d}}_{m_r} + \check{\mathbf{v}}_{m_r}^{(l)}) \\ \sqrt{\rho_4/2}(\check{\mathbf{u}}_s^{(l+1)} + \check{\mathbf{v}}_s^{(l)}) \\ \sqrt{\rho_5/2}(\check{\mathbf{g}}_c + \check{\mathbf{v}}_c^{(l)}) \end{bmatrix}, \ \check{\mathbf{B}} = \begin{bmatrix} \sqrt{\rho_1/2}[\mathbf{I}_{2NPQ}, \mathbf{0}_{2NPQ \times 2NP}] \\ \sqrt{\rho_2/2}[\check{\mathbf{B}}_{m_t}^{\mathrm{T}}, \mathbf{0}_{2PQ \times 2NP}] \\ \sqrt{\rho_3/2}[\mathbf{0}_{2P \times 2NPQ}, \check{\mathbf{B}}_{m_r}^{\mathrm{T}}] \\ \sqrt{\rho_4/2}\check{\mathbf{B}}_s^{\mathrm{T}} \\ \sqrt{\rho_5/2}[\check{\mathbf{B}}_c^{\mathrm{T}}, \mathbf{0}_{3KPQ \times 2NP}] \end{bmatrix}.$$

In $(\mathcal{P}_3')$, the $l_0$-norm in the objective function remains non-convex. To handle this non-convexity, we introduce a set of auxiliary variables $\mathbf{f}_n$ $(1 \leqslant n \leqslant N)$, and equivalently reformulate $(\mathcal{P}_3')$ as follows:

$$(\mathcal{P}_3'') \quad \min_{\mathbf{f}_n, n=1,\ldots,N, \check{\mathbf{w}}} \sum_{n=1}^{N} \mathcal{I}(||\mathbf{f}_n||_2^2) + ||\check{\mathbf{h}} - \check{\mathbf{B}}\check{\mathbf{w}}||_2^2 \tag{55}$$

$$\text{s.t. } \mathbf{f}_n = \left(\mathbf{I}_{2(PQ+P)} \otimes \mathbf{e}_n\right)^{\mathrm{T}} \check{\mathbf{w}}, \ n = 1, \ldots, N, \tag{55a}$$

where $\mathcal{I}(||\mathbf{f}_n||_2^2)$ returns "1" if $||\mathbf{f}_n||_2^2 \neq 0$, and "0" otherwise. Problem $(\mathcal{P}_3'')$ can also be solved using the ADMM

method. By incorporating (55a) into the objective function, we obtain the following augmented Lagrangian function:

$$\mathcal{L}_{P_3}(\check{\mathbf{w}}, \mathbf{f}_n, \boldsymbol{\iota}_n) = \sum_{n=1}^{N} \mathcal{I}(||\mathbf{f}_n||_2^2) + ||\check{\mathbf{h}} - \check{\mathbf{B}}\check{\mathbf{w}}||_2^2 + \frac{\rho_6}{2}\left(\sum_{n=1}^{N} ||\mathbf{f}_n - \left(\mathbf{I}_{2(PQ+P)} \otimes \mathbf{e}_n\right)^{\mathrm{T}} \check{\mathbf{w}} + \boldsymbol{\iota}_n||_2^2\right), \tag{56}$$

where $\rho_6$ represents the penalty parameter, and $\boldsymbol{\iota}_n$ is the scaled dual variable. The detailed steps for the $(j+1)$-th iteration of the ADMM applied to $(\mathcal{P}_3'')$ are outlined below

$$\begin{cases} (\mathcal{P}_{3-1}) & \check{\mathbf{w}}^{(j+1)} = \underset{\check{\mathbf{w}}}{\operatorname{argmin}}\ \mathcal{L}_{P_3}(\check{\mathbf{w}}, \mathbf{f}_n^{(j)}, \boldsymbol{\iota}_n^{(j)}), \\ (\mathcal{P}_{3-2}) & \mathbf{f}_n^{(j+1)} = \underset{\mathbf{f}_n}{\operatorname{argmin}}\ \mathcal{L}_{P_3}(\check{\mathbf{w}}^{(j+1)}, \mathbf{f}_n, \boldsymbol{\iota}_n^{(j)}), \\ (\mathcal{P}_{3-3}) & \boldsymbol{\iota}_n^{(j+1)} = \boldsymbol{\iota}_n^{(j)} + \mathbf{f}_n^{(j+1)} - \left(\mathbf{I}_{2(PQ+P)} \otimes \mathbf{e}_n\right)^{\mathrm{T}} \check{\mathbf{w}}^{(j+1)}. \end{cases} \tag{57}$$

As for $(\mathcal{P}_{3-1})$, by dropping the terms independent of the variable $\check{\mathbf{w}}$, it can be simplified to

$$(\mathcal{P}_{3-1}) \quad \min_{\check{\mathbf{w}}} ||\check{\mathbf{h}} - \check{\mathbf{B}}\check{\mathbf{w}}||_2^2 + \frac{\rho_6}{2}||\check{\mathbf{f}}^{(j)} - \check{\mathbf{w}} + \check{\boldsymbol{\iota}}^{(j)}||_2^2, \tag{58}$$

where $\check{\mathbf{f}}^{(j)} = \mathrm{vec}([\mathbf{f}_1^{(j)}, \mathbf{f}_2^{(j)}, \ldots, \mathbf{f}_N^{(j)}]^{\mathrm{T}})$ and $\check{\boldsymbol{\iota}}^{(j)} = \mathrm{vec}([\boldsymbol{\iota}_1^{(j)}, \boldsymbol{\iota}_2^{(j)}, \ldots, \boldsymbol{\iota}_N^{(j)}]^{\mathrm{T}})$. The solution to $(\mathcal{P}_{3-1})$ is given by

$$\check{\mathbf{w}}^{(j+1)} = \left(\check{\mathbf{B}}^{\mathrm{H}}\check{\mathbf{B}} + \frac{\rho_6}{2}\mathbf{I}_{2N(PQ+P)}\right)^{-1}\left(\check{\mathbf{B}}^{\mathrm{H}}\check{\mathbf{h}} + \frac{\rho_6}{2}\check{\mathbf{f}}^{(j)} + \frac{\rho_6}{2}\check{\boldsymbol{\iota}}^{(j)}\right). \tag{59}$$

When updating $\mathbf{f}_n$, ignoring the constant term, $(\mathcal{P}_{3-2})$ can be simplified as

$$(\mathcal{P}_{3-2}) \quad \min_{\mathbf{f}_n, n=1,\ldots,N} \sum_{n=1}^{N}\left(\mathcal{I}(||\mathbf{f}_n||_2^2) + \frac{\rho_6}{2}||\mathbf{f}_n - \left(\mathbf{I}_{2(PQ+P)} \otimes \mathbf{e}_n\right)^{\mathrm{T}} \check{\mathbf{w}}^{(j+1)} + \boldsymbol{\iota}_n^{(j)}||_2^2\right). \tag{60}$$

Since the optimization of $\mathbf{f}_n$ in $(\mathcal{P}_{3-2})$ is independent across different $n$, the variables can be optimized independently. Specifically, $(\mathcal{P}_{3-2})$ is equivalent to

$$(\mathcal{P}_{3-2}') \quad \min_{\mathbf{f}_n} \mathcal{I}(||\mathbf{f}_n||_2^2) + \frac{\rho_6}{2}||\mathbf{f}_n - \left(\mathbf{I}_{2(PQ+P)} \otimes \mathbf{e}_n\right)^{\mathrm{T}} \check{\mathbf{w}}^{(j+1)} + \boldsymbol{\iota}_n^{(j)}||_2^2. \tag{61}$$

Accordingly, $\mathbf{f}_n$ is updated according to

$$\mathbf{f}_n^{(j+1)} = \begin{cases} \left(\mathbf{I}_{2(PQ+P)} \otimes \mathbf{e}_n\right)^{\mathrm{T}} \check{\mathbf{w}}^{(j+1)} - \boldsymbol{\iota}_n^{(j)}, & \text{if } ||\left(\mathbf{I}_{2(PQ+P)} \otimes \mathbf{e}_n\right)^{\mathrm{T}} \check{\mathbf{w}}^{(j+1)} - \boldsymbol{\iota}_n^{(j)}||_2^2 \geqslant \frac{2}{\rho_6}, \\ \mathbf{0}_{2(PQ+P)}, & \text{if } ||\left(\mathbf{I}_{2(PQ+P)} \otimes \mathbf{e}_n\right)^{\mathrm{T}} \check{\mathbf{w}}^{(j+1)} - \boldsymbol{\iota}_n^{(j)}||_2^2 < \frac{2}{\rho_6}. \end{cases} \tag{62}$$

And thus $\mathbf{z}^{(j+1)}[n]$ can be calculated per $\mathbf{z}^{(j+1)}[n] = ||\mathbf{f}_n^{(j+1)}||_2^2$.

### 5.4 Solution to $(\mathcal{P}_4)$

Ignoring the constant terms in the objective function, problem $(\mathcal{P}_4)$ reduces to the following form:

$$(\mathcal{P}_4) \quad \min_{D_{m_t}} -D_{m_t} + \frac{\rho_2}{2}||D_{m_t}\mathbf{1}_{2PQ} - \check{\mathbf{B}}_{m_t}^{\mathrm{T}}\check{\mathbf{w}}_t^{(l+1)} + \check{\mathbf{v}}_{m_t}^{(l)}||_2^2. \tag{63}$$

The closed-form solution for updating $D_{m_t}$ can be expressed as

$$D_{m_t}^{(l+1)} = \frac{\rho_2 \mathrm{Re}\left(\mathbf{1}_{2PQ}^{\mathrm{T}}(\check{\mathbf{B}}_{m_t}^{\mathrm{T}}\check{\mathbf{w}}_t^{(l+1)} - \check{\mathbf{v}}_{m_t}^{(l)})\right) + 1}{2\rho_2 PQ}. \tag{64}$$

### 5.5 Computational complexity

The total number of transmit and receive sidelobe and cross-polarization constraints is denoted by

$$\check{S}_{\mathrm{tot}} = \check{S}_{t\text{-co}} + \check{S}_{t\text{-cr}} + \check{S}_{r\text{-co}} + \check{S}_{r\text{-cr}}, \tag{65}$$

**Table 1** Radar operating parameters.

| Parameter | Value | Parameter | Value |
|---|---|---|---|
| Working frequency (GHz) | 2.765 | Accumulated pulse count | 72 |
| Pulse width (μs) | 1.57 | Scanning beam width (°) | 2 |
| Pulse repetition frequency (Hz) | 1014 | Distance resolution (m) | 250 |

where the individual terms are defined in (38) and (39). The numbers of outer ADMM iterations and inner ADMM iterations for solving $(\mathcal{P}_3)$ are denoted by $\kappa_{\text{out}}$ and $\kappa_{\text{in}}$, respectively. The updates in $(\mathcal{P}_1)$, $(\mathcal{P}_2)$, $(\mathcal{P}_4)$, and $(\mathcal{P}_5)$ mainly involve structured matrix-vector multiplications and element-wise or linear operations, with complexities $\mathcal{O}(N\check{S}_{\text{tot}})$, $\mathcal{O}(NPQ)$, $\mathcal{O}(NPQ)$, and $\mathcal{O}(N[\check{S}_{\text{tot}} + KPQ + PQ + P])$, respectively.

The dominant cost arises from $(\mathcal{P}_3)$. By exploiting the block-diagonal and Kronecker structures in (36)–(41), the matrix inversion in $(\mathcal{P}_{3-1})$ can be efficiently implemented through factorizations of $2P$ distinct $2N \times 2N$ coefficient matrices. Since these coefficient matrices remain unchanged throughout the ADMM iterations, the factorizations only need to be computed once, with complexity $\mathcal{O}(PN^3)$. Each subsequent $(\mathcal{P}_{3-1})$ update requires $\mathcal{O}(N^2P(Q+1))$, while $(\mathcal{P}_{3-2})$ and $(\mathcal{P}_{3-3})$ both require $\mathcal{O}(NP(Q+1))$.

Therefore, retaining the dominant terms, the overall computational complexity is

$$\mathcal{O}\left\{PN^3 + \kappa_{\text{out}}[N(\check{S}_{\text{tot}} + KPQ + PQ + P) + \kappa_{\text{in}}N^2P(Q+1)]\right\}. \tag{66}$$

For traditional sparse-array design methods, exhaustive search requires examining up to $2^N$ antenna configurations, with the corresponding joint transmit-receive beamforming problem solved for each configuration, resulting in a complexity of up to $\mathcal{O}(2^N[2NP(Q+1)+1]^{3.5})$ in the worst case. Heuristic-search methods reduce the number of candidate configurations but still require repeated beamforming optimization. For successive convex approximation (SCA)-based methods, each approximation requires solving a convex subproblem using a computationally demanding interior-point method, leading to a complexity of approximately $\mathcal{O}(\kappa_{\text{SCA}}[2NP(Q+1)+1]^{3.5})$, where $\kappa_{\text{SCA}}$ denotes the number of SCA iterations. In contrast, the proposed ADMM, as characterized in (66), greatly reduces the computational complexity.

## 6 Simulation results

This section evaluates the proposed sparse dual-function polarized conformal weather radar system with integrated communications via simulations. We first examine the transmit and receive beampattern characteristics of the designed sparse conformal array and its information embedding capability. Simulated multi-channel dual-polarized meteorological echoes, generated from the public WSR-88D dataset, are then used to validate the joint sensing and communication performance of the proposed dual-functional system.

### 6.1 Performance of the designed sparse array

We first validate the proposed sparse array design via its transmit/receive beampatterns and information embedding capability. Consider a cylindrical airship surface with a radius of curvature of 3 m. A $50 \times 50$ uniform conformal planar array (UCPA) with half-wavelength spacing is centered on the airship side, from which a sparse array is formed by selecting the minimum number of elements. The radar operating parameters are listed in Table 1.

Assume that each antenna is equipped with an ideal $Y$-dipole at its $V$-port and an ideal $X$-dipole at its $H$-port. The vertical and horizontal polarization radiation patterns for the $Y$-dipole are shown in Figures 2(c) and (d), with those for the $X$-dipole shown in Figures 2(a) and (b). The detection region covers an elevation of 91° and azimuth range from 60° to 120°, with two downlink users at $(120°, 60°)$ and $(150°, 90°)$ (given as elevation, azimuth). The radar scans with a 2° interval and 2° beamwidth. For co-polarization transmit beampatterns of both channels, the normalized PSLL (excluding communication directions) remains below −15 dB across all detection angles and symbol-embedding conditions, with normalized cross-polarization gain below −40 dB. On the receive side, we set $D_{m_r} = 1$, $D_{s_r\text{-co}} = 0.1585$ and $D_{s_r\text{-cr}} = 0.0100$, requiring the normalized co-polarization PSLL below −16 dB and the normalized cross-polarization gain below −40 dB. QPSK with dictionary $\bar{\mathbb{D}}_c = \{0, \pi/2, \pi, 3\pi/2\}$ is applied, achieving 30 dBW radiated power toward users. With two users, the joint dictionary $\mathbb{D}_c = \bar{\mathbb{D}}_c^3 \times \bar{\mathbb{D}}_c^3$ yields $4^6$ distinct symbols.

Applying the joint design method in Section 5, we perform an integrated optimization covering 31 transmit scanning angles and $4^6$ symbol combinations, along with 31 receive beampatterns per scanning angle. This yields

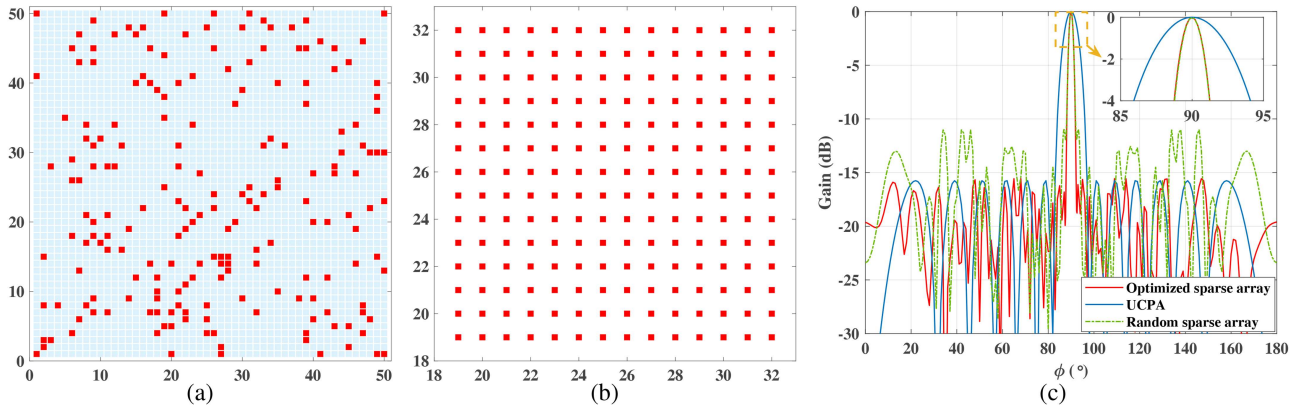


**Figure 3** (Color online) Configurations of (a) the optimized sparse conformal array and (b) the UCPA. (c) Comparison of transmit beampatterns.

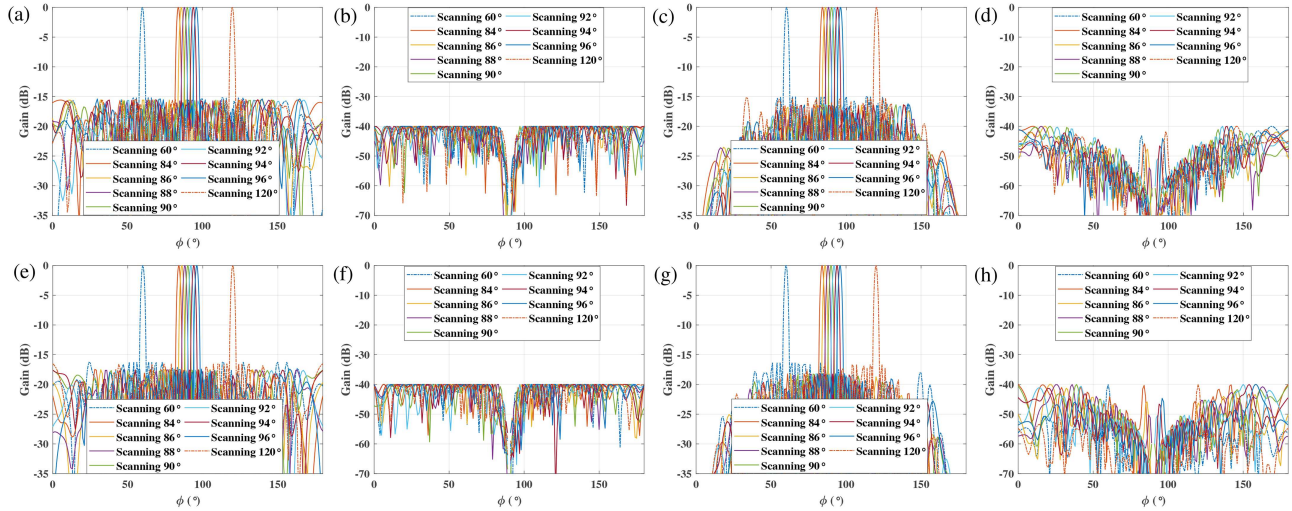


**Figure 4** (Color online) Scanning beampatterns: (a)–(d) transmit; (e)–(h) receive. (a) and (e) $V$-port: co-polarization; (b) and (f) $V$-port: cross-polarization; (c) and (g) $H$-port: co-polarization; (d) and (h) $H$-port: cross-polarization.

the optimal sparse array shown in Figure 3(a), comprising 196 selected elements. The normalized co- and cross-polarization beampatterns along the 91° elevation cut are presented in Figure 4, with Figures 4(a)–(d) for transmission and Figures 4(e)–(h) for reception. The co-polarization transmit beampatterns of the $V$- and $H$-ports (Figures 4(a) and (c)) exhibit well-defined directivity across all scanning angles, with a 3 dB mainlobe beamwidth of approximately 2°—precisely covering one angle bin—and sidelobe levels below −15 dB. Their corresponding cross-polarization patterns (Figures 4(b) and (d)) remain below −40 dB, effectively suppressing cross-polar interference. At the receive end, the co-polarization beampatterns (Figures 4(e) and (g)) achieve the same 2° 3 dB beamwidth and a low sidelobe profile with PSLL of −16 dB, while the cross-polarization patterns (Figures 4(f) and (h)) stay below −40 dB across the entire observation region, ensuring robust rejection of cross-polar components.

We then plot, as defined in (25), (29) and (30), the transmit power beampatterns for the $X$-, $Y$-, and $Z$-polarization components along the elevation slices corresponding to the two communication users (120° and 150°), with results shown in Figure 5. Figures 5(a)–(f) depict the amplitude responses, while Figures 5(g)–(l) show the corresponding phase responses. In the directions of the two users, the transmit power along all three polarization components is consistently 30 dBW, and the phases are precisely modulated to embed the four QPSK states 0, $\pi/2$, $\pi$, and $3\pi/2$. These results confirm that communication information is accurately embedded into the synthesized beampatterns, enabling reliable communication with both users. To more intuitively illustrate the transmit power distribution, we take the case where the scanning angle is set to an elevation of 91° and an azimuth of 90°, with both embedded communication symbols being "0", as an example. The 3D normalized transmit co-polarization beampatterns for the $H$- and $V$-ports are plotted in Figure 6. The transmit power is concentrated in the scanning direction and the two communication user directions, with sidelobe levels below −15 dB.

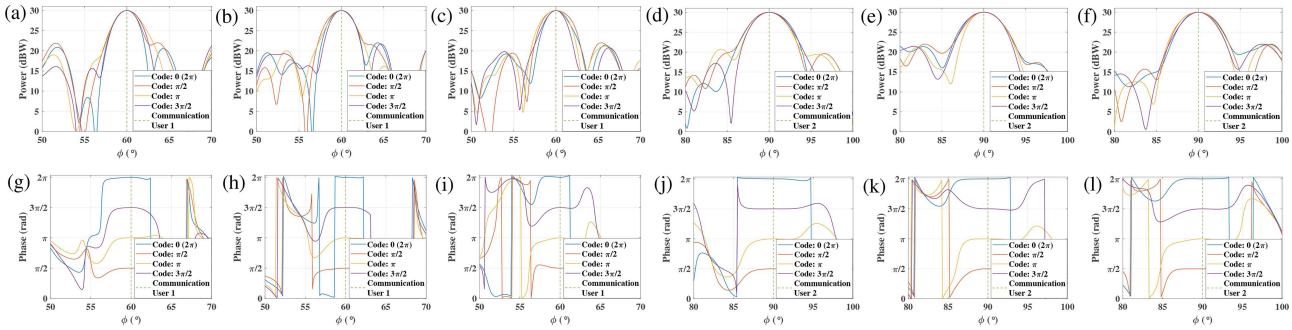


**Figure 5** (Color online) Transmit beampatterns for two communication users: (a)–(f) magnitude responses; (g)–(l) phase responses. (a) and (g) User 1: $X$-direction; (b) and (h) User 1: $Y$-direction; (c) and (i) User 1: $Z$-direction; (d) and (j) User 2: $X$-direction; (e) and (k) User 2: $Y$-direction; (f) and (l) User 2: $Z$-direction.

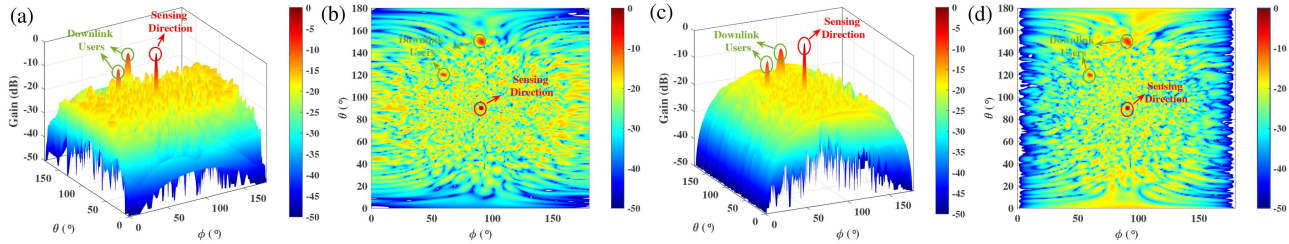


**Figure 6** (Color online) 3D co-polarization beampatterns while scanning azimuth angle 90°. (a) $V$-port; (b) $V$-port (top view); (c) $H$-port; (d) $H$-port (top view).

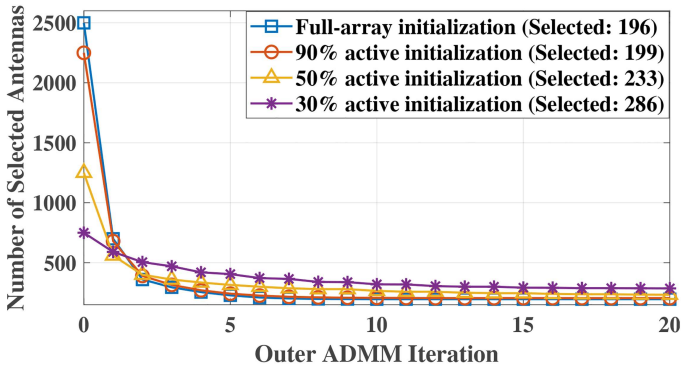


**Figure 7** (Color online) Convergence behavior of the proposed ADMM under different antenna-selection initializations.

The proposed optimized sparse array is also compared with a UCPA with half-wavelength spacing (Figure 3(b)) and a randomly selected sparse array. Figure 3(c) compares their normalized transmit co-polarization beampatterns along the 91° elevation cut. The optimized sparse array achieves superior beam focusing and PSLL performance. In contrast, the UCPA exhibits a 6° 3 dB beamwidth, causing energy leakage between adjacent angle bins, while the random sparse array has a PSLL of approximately −11 dB—significantly worse than the optimized design.

We further investigate the convergence behavior of the proposed ADMM under different initializations of the antenna selection variable. Specifically, full-array initialization and random initializations with 90%, 50%, and 30% active antennas are considered. As shown in Figure 7, initializations with more active antennas, i.e., the full-array and 90%-active cases, generally converge faster and yield sparser final arrays. In contrast, initializations with fewer active antennas, i.e., the 50%- and 30%-active cases, tend to converge more slowly and result in larger final array sizes. This is because denser initializations reduce the bias toward a particular sparse configuration, whereas sparser initializations make the iterations more dependent on the initial active set and more susceptible to less favorable solutions. Accordingly, the full-array configuration is adopted in the following simulations.

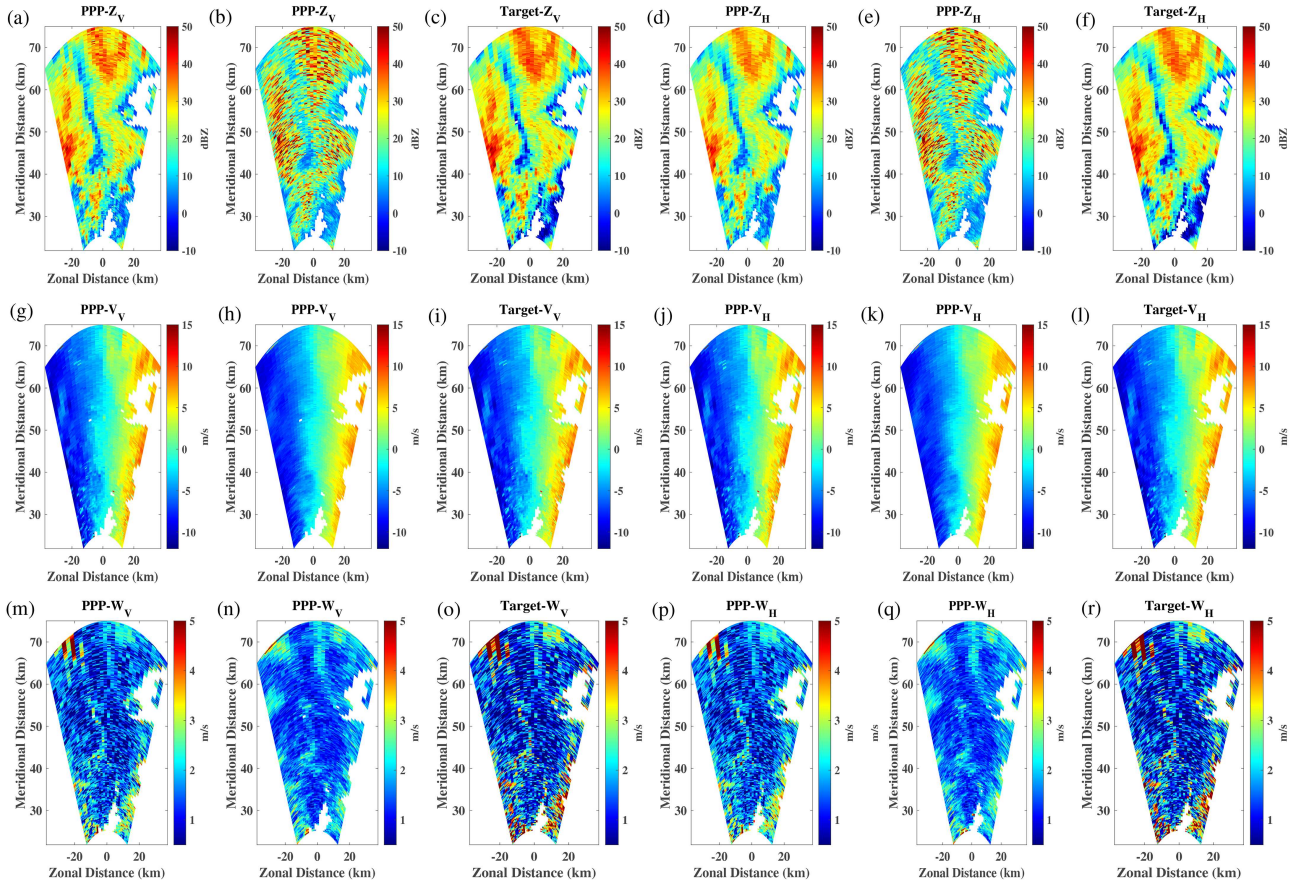


**Figure 8** (Color online) Reflectivity factor ($Z_{V/H}$): (a)–(c) $V$-port, (d)–(f) $H$-port; radial velocity ($V_{V/H}$): (g)–(i) $V$-port, (j)–(l) $H$-port; spectrum width ($W_{V/H}$): (m)–(o) $V$-port, (p)–(r) $H$-port. (a), (d), (g), (j), (m), and (p) Optimized array; (b), (e), (h), (k), (n), and (q) UCPA; (c), (f), (i), (l), (o), and (r) WSR-88D.

### 6.2 Dual-function evaluation using simulated multi-channel dual-polarized weather echoes

In this subsection, we first simulate multi-channel dual-polarized weather radar echoes using meteorological parameters from the public WSR-88D dataset. For each range-angle bin, the echo power spectrum is modeled as Gaussian based on the radar radial velocity and spectral width. Polarization parameters, including differential reflectivity, differential phase, and correlation coefficient, are derived from the WSR-88D dataset. For a given receive antenna, its received echo power for both the $H$- and $V$-channels can be calculated based on these parameters, the transmit array gain, and the antenna's own receive gain (noting that for conformal arrays, different receive antennas exhibit different gains toward the same meteorological target). To capture the random fluctuation characteristics of meteorological scatterers, correlated complex random sequences are generated for $H$- and $V$-channels using a specified zero-lag correlation coefficient. These sequences are then shaped in the frequency domain to match the Gaussian power spectrum, with differential propagation phase applied. Finally, time-domain echo sequences are obtained via inverse Fourier transform and addition of Gaussian noise, yielding the echo for one receive antenna. Repeating this process across all receive antennas generates the multi-channel dual-polarized received data.

We further validate the meteorological sensing performance of the optimized sparse array by emulating the signal processing chain with simulated weather echoes. WSR-88D radar measurements are adopted as ground truth, with the UCPA in Figure 3(b) serving as a benchmark. The retrieved reflectivity factor, radial velocity, and spectrum width for both $H$- and $V$-channels are shown in Figures 8(a)–(f), (g)–(l), and (m)–(r), respectively. The estimated dual-polarized parameters—differential reflectivity ($Z_{DR}$), differential propagation phase ($\phi_{DP}$), and copolar correlation coefficient ($\rho_{HV}$)—are presented in Figures 9(a)–(c), (d)–(f), and (g)–(i), respectively. Results demonstrate that the optimized sparse array accurately retrieves the actual meteorological scenario. For instance, as shown in Figures 8(a) and (c), the reflectivity factor estimated by the optimized sparse array closely matches the ground truth, whereas the UCPA exhibits considerable energy leakage between adjacent angle bins due to its overly wide mainlobe, leading to substantial estimation errors. These findings highlight the clear advantage of the

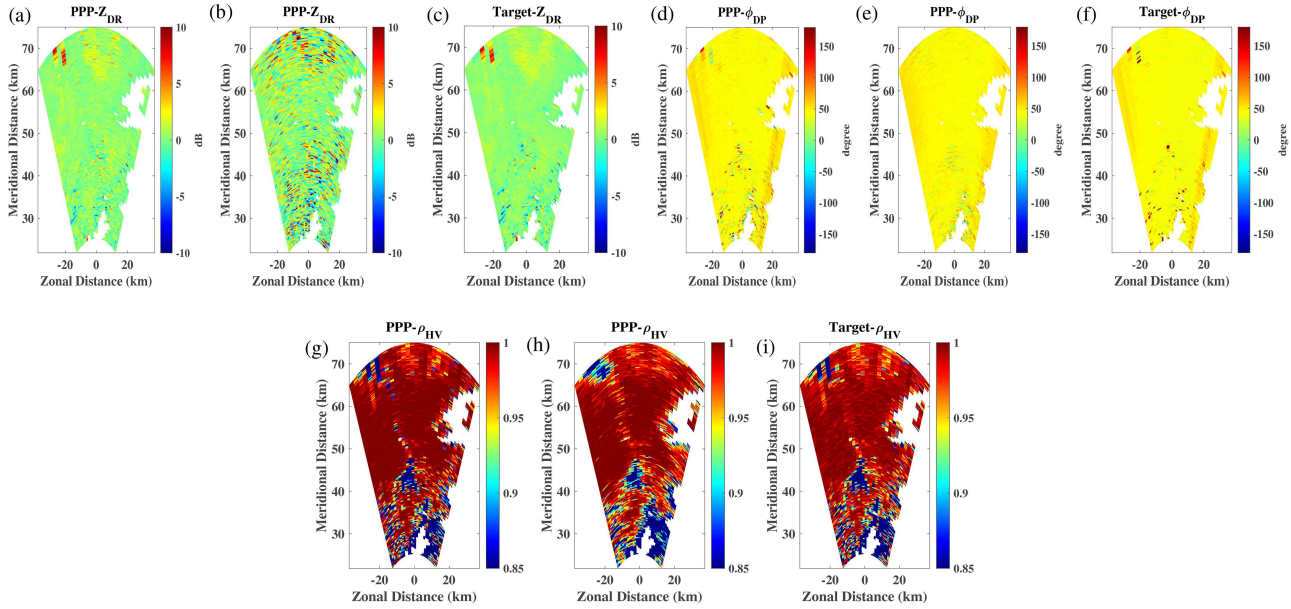


**Figure 9** (Color online) (a)–(c) Differential reflectivity ($Z_{DR}$), (d)–(f) differential propagation phase ($\phi_{DP}$), (g)–(i) copolar correlation coefficient ($\rho_{HV}$). (a), (d), and (g) Optimized array; (b), (e), and (h) UCPA; (c), (f), and (i) WSR-88D.

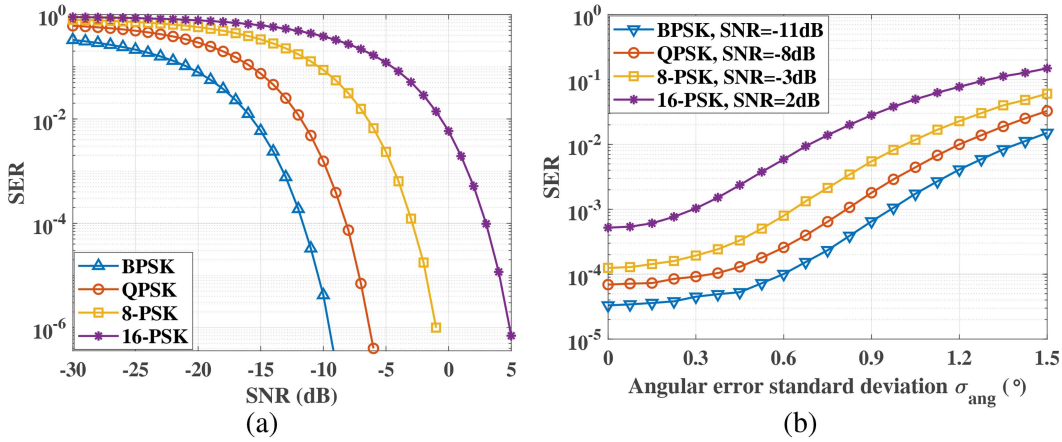


**Figure 10** (Color online) (a) Average user SER versus SNR under different signaling schemes; (b) average SER versus angular error standard deviation, i.e., $\sigma_{\text{ang}}$, under different signaling schemes.

optimized sparse array in angular resolution and meteorological parameter retrieval accuracy.

For communications, the two users decode information from the $X$-, $Y$-, and $Z$-channels using the method in Section 3. With 100 snapshots sampled per pulse in matched filtering, we compute the average symbol error rate (SER) for both users across the three channels under BPSK, QPSK, 8-PSK, and 16-PSK, maintaining the same transmit power for all schemes. Figure 10(a) shows the average SER versus received signal-to-noise ratio (SNR). The results confirm reliable communication—e.g., for QPSK, a SER below $10^{-5}$ is achieved when received SNR exceeds $-7$ dB.

To further evaluate the communication robustness against airship vibration, we consider residual beam-pointing errors after attitude compensation. Since large-scale attitude deviations caused by atmospheric turbulence and wind gusts can be compensated using real-time attitude and navigation information [46–49], only the remaining small residual perturbations are considered. The elevation and azimuth errors are modeled as independent zero-mean Gaussian variables, i.e., $\Delta\theta, \Delta\phi \sim \mathcal{N}(0, \sigma_{\text{ang}}^2)$, where $\sigma_{\text{ang}}$ denotes the angular error standard deviation. The actual pointing direction is thus given by $\tilde{\theta} = \theta + \Delta\theta$ and $\tilde{\phi} = \phi + \Delta\phi$, with $\sigma_{\text{ang}}$ ranging from 0° to 1.5°. As shown in Figure 10(b), the average SER over the $X$-, $Y$-, and $Z$-polarization channels increases with $\sigma_{\text{ang}}$ for all signaling schemes. When $\sigma_{\text{ang}} < 0.6°$, the SER degradation remains limited, particularly for BPSK and QPSK, demonstrating good robustness to small residual angular perturbations.

## 7 Conclusion

This paper proposed an airship-borne dual-polarized conformal ISAC system to serve the LAE, enabling reliable communications and high-resolution meteorological scanning via integrating sparse array optimization with joint transmit-receive beamforming. For the first time, sparse array design was investigated within a dual-polarized conformal architecture. We established a conformal meteorological detection model with directive antenna patterns and proposed a polarization-based transmit beampattern modulation scheme. The joint design was formulated as a multivariate combinatorial optimization problem and solved via ADMM, yielding a unified sparse layout valid across all scanning angles and communication symbols. Simulations validated the proposed ISAC system. Multi-channel weather echoes were simulated using WSR-88D data to assess system performance. Compared to a UCPA with the same element count, the optimized sparse array demonstrated superior detection and communication capabilities.

**Acknowledgements** The work was supported by National Natural Science Foundation of China (Grant Nos. U2333212, 61827901) and Beijing Natural Science Foundation (Grant No. L244045).

**References**

1 Luo G, Li J, Zhang Q, et al. Toward low-altitude airspace management and UAV operations: requirements, architecture and enabling technologies. IEEE Wireless Commun, 2026, 33: 45–55
2 Wu F, Luo Y, Xu Y, et al. Energy minimization for fixed-wing AAV inspection system in multi-hangar and windy environment. IEEE Trans Veh Technol, 2025, 74: 17840–17853
3 Ma D, Tang J, Zhang Q, et al. Integrated sensing and communications network design and key technologies for low-altitude economy. China Commun, 2025, 22: 81–102
4 Kurdzo J M, Donovan M F, Cho J Y N, et al. Impact of WSR-88D MESO-SAILS usage on MRMS-based quantitative precipitation estimation. In: Proceedings of the 2024 IEEE Radar Conference (RadarConf24), 2024. 1–6
5 Pulkkinen S, Chandrasekar V, von Lerber A, et al. Nowcasting of convective rainfall using volumetric radar observations. IEEE Trans Geosci Remote Sens, 2020, 58: 7845–7859
6 An M, Yin J, Wang T, et al. Quantitative impacts of different polarization operating modes and waveforms on weather observables for polarimetric phased array radar. IEEE Trans Geosci Remote Sens, 2024, 62: 1–22
7 Palmer R D, Schvartzman D. Emerging trends in radar: phased arrays for weather observations. IEEE Aerosp Electron Syst Mag, 2025, 40: 60–64
8 Fulton C, Salazar J L, Zhang Y, et al. Cylindrical polarimetric phased array radar: beamforming and calibration for weather applications. IEEE Trans Geosci Remote Sens, 2017, 55: 2827–2841
9 Jia Y, Chen H, He M, et al. Joint array design and pattern synthesis optimization for flexible conformal arrays. IEEE Trans Antennas Propagat, 2024, 72: 3104–3118
10 Zhang X, Gao X, Bu X, et al. An improved snake optimization algorithm for sparse conformal array beamforming. IEEE Trans Veh Technol, 2024, 73: 8542–8548
11 Sun Z, Hu C, Cui K, et al. Extracting bird and insect migration echoes from single-polarization weather radar data using semi-supervised learning. IEEE Trans Geosci Remote Sens, 2024, 62: 1–12
12 Notaros B M. Polarimetric weather radar: overview of principles and applications. IEEE Antennas Propag Mag, 2022, 64: 43–54
13 Chandrasekar V, Yoshikawa E, Dwarakanath V, et al. Considerations for dual-polarization measurements from an airborne phased array Doppler weather radar. In: Proceedings of the 2024 IEEE International Symposium on Phased Array Systems and Technology (ARRAY), 2024. 1–6
14 Schvartzman D, Zrnic D. Dual-PRF processing algorithm for enhanced polarimetric measurements in weather radar. IEEE Trans Geosci Remote Sens, 2025, 63: 1–20
15 Zhang J, Chen H, Han L. An investigation of a probabilistic nowcast system for dual-polarization radar applications. In: Proceedings of the 2020 IEEE International Geoscience and Remote Sensing Symposium (IGARSS), 2020. 5294–5297
16 Dong X, Zhao X, Shao N, et al. Improved spectrum width estimator using multi-lag correlation function in the alternate transmission mode for polarimetric weather radar. IEEE Trans Geosci Remote Sens, 2024, 62: 1–18
17 Yin J, Hoogeboom P, Unal C, et al. Radio frequency interference characterization and mitigation for polarimetric weather radar: a study case. IEEE Trans Geosci Remote Sens, 2022, 60: 1–16
18 Zrnić D S, Melnikov V M. Estimation of transmitted differential phase on dual-polarization radars. J Atmos Ocean Tech, 2023, 40: 1221–1239
19 Schvartzman D, Zrnić D, Cheong B, et al. Measurement of transmitted differential phase on polarimetric radars. IEEE Geosci Remote Sens Lett, 2024, 21: 1–5
20 Schvartzman D, Palmer R D, Herndon M, et al. Enhanced weather surveillance capabilities with multiple simultaneous transmit beams. Trans Rad Sys, 2025, 3: 272–289
21 Chen Z, Hu W, Lin C, et al. Ultrawideband, dual-polarized, high-isolation conformal phase array: design and implementation. Antennas Wirel Propag Lett, 2025, 24: 2789–2793
22 Dohmen C, Odendaal J W, Joubert J. Synthesis of conformal arrays with optimized polarization. IEEE Trans Antennas Propagat, 2007, 55: 2922–2925
23 Jia Y, Wang W Q, Zhang X C, et al. Generalized ambiguity function analysis and geometry parameter optimization for flexible conformal array-MIMO radar. IEEE Trans Aerosp Electron Syst, 2024, 60: 1334–1350
24 Zhou C, You C, Zhang H, et al. Sparse array enabled near-field communications: beam pattern analysis and hybrid beamforming design. IEEE Trans Wireless Commun, 2025, 24: 10261–10277
25 He J, De Maio A, Huang Y. Emerging trends in radar: robust sparse beamforming for radar array processing. IEEE Aerosp Electron Syst Mag, 2025, 40: 30–34
26 Wang X, Zhai W, Wang X, et al. Wideband near-field integrated sensing and communication with sparse transceiver design. IEEE J Sel Top Signal Process, 2024, 18: 662–677
27 Kikuchi H, Hobara Y, Ushio T. Compressive sensing to reduce the number of elements in a linear antenna array with a phased array weather radar. IEEE Trans Geosci Remote Sens, 2022, 60: 1–10
28 Kawaguchi T, Shinotsuka K, Malterer S. Experimental verification of rainfall impact on sparse array radar. In: Proceedings of the 2024 IEEE Radar Conference (RadarConf24), 2024. 1–6
29 Wang X, Huang J, Wang X, et al. Optimal sparse array design for airborne weather radar with integrated communications. IEEE Trans Aerosp Electron Syst, 2025, 61: 4238–4254
30 Wang X, Zhai W, Wang X, et al. Wideband near-field integrated sensing and communications: a hybrid precoding perspective. IEEE Signal Process Mag, 2025, 42: 88–105

31 Zhai W, Wang X, Zhou C, et al. Dual-functional IRS design for ISAC via reinforcement learning in unknown environment. IEEE Trans Aerosp Electron Syst, 2025, 61: 17785–17803
32 Koivunen V, Keskin M F, Wymeersch H, et al. Multicarrier ISAC: advances in waveform design, signal processing, and learning under nonidealities. IEEE Signal Process Mag, 2024, 41: 17–30
33 Liao Z T, Wu S F, Lee M C, et al. Design of joint transmit beamforming for multi-user MIMO-OFDM integrated sensing and communication systems. IEEE Trans Wireless Commun, 2025, 24: 6101–6117
34 Zhang R, Gong Y, Chen C, et al. Joint MMSE and CRB-based robust beamforming design for monostatic ISAC systems with channel uncertainty. IEEE Trans Commun, 2026, 74: 3120–3131
35 Li F Z, Ren Z C, Pan C H, et al. Cooperative sensing and communication beamforming design for low-altitude economy. Sci China Inf Sci, 2026, 69: 122304
36 Zeng F, Liu R Y, Sun X Y, et al. Multi-static ISAC based on network-assisted full-duplex cell-free networks: performance analysis and duplex mode optimization. Sci China Inf Sci, 2025, 68: 150303
37 Song X X, Fang Y, Wang F, et al. An overview on IRS-enabled sensing and communications for 6G: architectures, fundamental limits, and joint beamforming designs. Sci China Inf Sci, 2025, 68: 150301
38 Wang X, Gini F, Cai K. Reconfigurable integrated sensing and communications (RISAC): sparse MIMO and hybrid beamforming in far and near fields. Proc IEEE, 2026, 114: 93–120
39 Chen G, Zhang R, Guan X, et al. Movable antenna-enabled MIMO integrated sensing and communication: a unified mutual information framework. IEEE Trans Wireless Commun, 2026, 25: 14440–14454
40 Elbir A M, Celik A, Eltawil A M, et al. Index modulation for integrated sensing and communications: a signal processing perspective. IEEE Signal Process Mag, 2024, 41: 44–55
41 Wu K, Zhang J A, Huang X, et al. Frequency-hopping MIMO radar-based communications: an overview. IEEE Aerosp Electron Syst Mag, 2022, 37: 42–54
42 Xu J, Wang X, Aboutanios E, et al. Hybrid index modulation for dual-functional radar communications systems. IEEE Trans Veh Technol, 2023, 72: 3186–3200
43 Zhai W, Wang X, Cao X, et al. Reinforcement learning based dual-functional massive MIMO systems for multi-target detection and communications. IEEE Trans Signal Process, 2023, 71: 741–755
44 Wu H, Jin B, Zhang Z, et al. Robust transmit beamforming in MIMO dual-functional radar-communication systems for unidirectional multi-user communication. IEEE Trans Veh Technol, 2025, 74: 4307–4318
45 Hassanien A, Amin M G, Aboutanios E, et al. Dual-function radar communication systems: a solution to the spectrum congestion problem. IEEE Signal Process Mag, 2019, 36: 115–126
46 Feng L, Hu J, Feng K, et al. A method of attitude error compensation for airship-borne meteorological radar. In: Proceedings of the 2022 International Conference on Radar Systems (RADAR 2022), 2022. 523–527
47 Xing M, Jiang X, Wu R, et al. Motion compensation for UAV SAR based on raw radar data. IEEE Trans Geosci Remote Sens, 2009, 47: 2870–2883
48 Rosen P A, Hensley S, Wheeler K, et al. UAVSAR: a new NASA airborne SAR system for science and technology research. In: Proceedings of the 2006 IEEE Radar Conference, 2006. 1–8
49 Schvartzman D, Torres S M, Yu T Y. Integration of the motion-compensated steering and distributed beams' techniques for polarimetric rotating phased array radar. IEEE Geosci Remote Sens Lett, 2022, 19: 1–5
50 Huang H, Wu L, Shankar B, et al. Sparse array design for dual-function radar-communications system. IEEE Commun Lett, 2023, 27: 1412–1416
51 Wen C, Huang Y, Peng J, et al. Reconfigurable sparse array synthesis with phase-only control via consensus-ADMM-based sparse optimization. IEEE Trans Veh Technol, 2021, 70: 6647–6661
52 Wang C, Chen H. Wideband sparse array synthesis with frequency-invariant pencil beampatterns using $l_0$-norm minimization. IEEE Trans Antennas Propagat, 2026, 74: 1551–1565